MNRAS 000, 1–18 (2024) Preprint 28 August 2024 Compiled using MNRAS LATEX style file v3.0

More than just a line: Implications of the shape and scatter of the flattening radial metallicity gradient of a NIHAO-UHD Milky Way analogue for studies of the Milky Way and other galaxies

Sven Buder,[1,2,5]⋆ Tobias Buck,[3,4] Qian-Hui Chen (陈千惠),[1,2] and Kathryn Grasha[1,2,5]
[1]*Research School of Astronomy & Astrophysics, Australian National University, ACT 2611, Australia*
[2]*Center of Excellence for Astrophysics in Three Dimensions (ASTRO-3D), Australia*
[3]*Universität Heidelberg, Interdisziplinäres Zentrum für Wissenschaftliches Rechnen, Im Neuenheimer Feld 205, D-69120 Heidelberg, Germany*
[4]*Universität Heidelberg, Zentrum für Astronomie, Institut für Theoretische Astrophysik, Albert-Ueberle-Strae 2, D-69120 Heidelberg, Germany*
[5]*Australian Research Council (ARC) Discovery Early Career Researcher Award (DECRA) Fellow*

Accepted YYYY Month DD. Received YYYY Month DD

ABSTRACT

Radial metallicity gradients in galaxies are crucial for understanding the processes of galaxy formation and its dynamical and chemical evolution. We use young stars and gas of a high-resolution simulation of a NIHAO-UHD Milky Way analogue galaxy to analyse four properties of the radial metallicity gradient, namely its linearity and scatter as well as its coherence with radial coverage, azimuth, and age. While a global linear fit with slope traces the gradient well, we find it to be too flat in the inner galaxy and too steep in the outer galaxy. An initially stepper but then flattening second order quadratic function provides a superior fit down to the smallest radial steps, where local enhancement varies. We correlate the enhancement deviations with spiral arms when tracing them across the Galactic position and age. The simulation further exhibits a steadily increasing spread in [Fe/H] even among the young stars from 0.01 dex in the inner galaxy to 0.14 dex at a radius 20 kpc coinciding with decreasing stellar density and increased flaring of stars towards higher heights with little correlation across the small age range of 1 Gyr. We conclude that future Galactic and extragalactic observational studies should test our theoretical prediction of a quadratic gradient function with their data to confirm or reject previous observational claims of a broken linear radial metallicity gradient proposed for the Milky Way and other spiral galaxies, as either function implies different dynamical and chemical galaxy formation and evolution scenarios.

Key words: cosmology: observations – Galaxy: structure – Galaxy: abundances – galaxies: structure – galaxies: abundances

1 INTRODUCTION

Understanding the radial metallicity gradient, defined as the change in heavy element abundance with galactocentric radius, in galaxies provides critical insights into their formation and evolutionary processes, such as inside-out formation, gas accretion, outflows, and radial migration (e.g. Quirk & Tinsley 1973; Tinsley 1980; Lacey & Fall 1985; Wyse & Silk 1989; Kauffmann 1996; Chiappini et al. 1997; Schönrich & Binney 2009; Moran et al. 2012; Bird et al. 2013). In this study, we analyze a simulated Milky Way analogue, aiming to uncover nuanced details of its radial metallicity gradient that might be obscured by observational limitations in our own and distant galaxies. By leveraging high-resolution simulations, we hope to bridge the gap between the detailed yet spatially confined observations of the Milky Way and the broader, but often less detailed, extragalactic observations. Our aim is to provide unique perspectives from simulations that can enhance the interpretative power of both Milky Way and extragalactic datasets, fostering a deeper understanding of galactic chemical evolution across different environments and epochs.

The decrease in metallicity with increasing distance from the Galactic center is well-established both theoretically (Larson 1976; Tinsley 1980; Chiosi 1980) and observationally in the Milky Way (Searle 1971; Janes 1979; Twarog et al. 1997) and other galaxies (e.g. Tinsley 1980; Zaritsky et al. 1994; Bresolin et al. 2012). The Milky Way, being the only galaxy where we can resolve millions of stars, provides a unique opportunity to study these gradients and deviations from them in detail. However, the specific shape and characteristics of this gradient remain somewhat unclear. Over two decades ago, Chiappini (2002) highlighted the contradictions in the observed shape, magnitude, and evolution of abundance gradients. Previous studies have for example claimed more intricate non-linear trends and bends in the gradient of the Milky Way (e.g. Donor et al. 2020) and other galaxies (e.g. Pilyugin 2003) or even sequences of shapes (Pilyugin et al. 2017; Pilyugin & Tautvaišienė 2024), which were fitted with different models (Rosales-Ortega et al. 2011; Bresolin et al. 2012), such as piecewise linear ones (e.g. Sánchez-Menguiano et al. 2016) or non-linear ones (e.g. Scarano & Lépine 2013).

The different shapes, including breaks of the gradient at specific radii, gave rise to a plethora of possible physical explanations, such as star formation efficiency variations and localised star formation bursts (Sánchez et al. 2014; Sánchez-Blázquez et al. 2014; Ho et al.

⋆ E-mail: sven.buder@anu.edu.au

2015), gas accretion and dilution at different rates (Bresolin et al. 2012; Sánchez et al. 2013; Belfiore et al. 2016; Sánchez-Menguiano et al. 2016), gas outflows and feedback (Lilly et al. 2013; Ma et al. 2017a), as well disk instabilities or local overdensities (Grand et al. 2016; Ho et al. 2017). In particular, Scarano & Lépine (2013) found that gradient break radii coincided with corotation radii of spiral arms.

Recent advancements in both computations and observations have significantly expanded our capabilities, for example in terms of observational data in the Milky Way by the *Gaia* mission (Gaia Collaboration et al. 2016), allowing for more detailed studies of these gradients. New suites of large-scale simulations now allow to gain insights into radial metallicity gradients across a range of simulated galaxies - including Milky Way analogues, thus posing the opportunity to revisit outstanding challenges of the detailed shape of the radial metallicity gradient.

For instance, Hogg et al. (2019) created an extensive metallicity map of the Milky Way using APOGEE and *Gaia* data, while Poggio et al. (2022) mapped young stars and found a metallicity excess around spiral arms (see also Zari et al. 2018, 2021; Poggio et al. 2021; Hackshaw et al. 2024). Similarly, Imig et al. (2023, among others) traced gradients across different stellar populations and ages, emphasizing the importance of considering radial migration effects (Binney & Tremaine 2008; Frankel et al. 2018, 2020). Historically, radial metallicity gradients have been measured using various stellar populations and gas tracers. Early evidence by Janes (1979) suggested a linear gradient on the order of

$$\frac{\mathrm{d[Fe/H]}}{\mathrm{d}R} = -0.05 \pm 0.01\,\mathrm{dex\,kpc^{-1}} \quad (1)$$

for the Milky Way which aligns with more recent measurements (Anders et al. 2017; Hayden et al. 2015). Estimated gradients also seem to be broadly consistent across different stellar tracers, such as young open clusters (e.g. Yong et al. 2012; Cunha et al. 2016; Magrini et al. 2017; Casamiquela et al. 2019; Donor et al. 2020; Spina et al. 2021; Myers et al. 2022), young hot (OB-type) stars (Zari et al. 2018, 2021; Poggio et al. 2021, 2022), field stars close to the Galactic plane (e.g. Bergemann et al. 2014) or Cepheids (Andrievsky et al. 2002a,b; Lemasle et al. 2007, 2013). However, these gradients are accompanied by significant spread in [Fe/H] of $0.1-0.15$ dex, as noted by Twarog (1980), which may imply a fine structure of the metallicity gradient (see Genovali et al. 2014).

Despite extensive observational efforts, several challenges persist for studies in the Milky Way:

- The completeness (or patchiness) of observed datasets remains a fundamental issue (Bergemann et al. 2014).
- How robustly can we use the incomplete data to predict substructure in the gradients, such as the need to actually fit two linear gradients with a break radius at corotation radius (Bresolin et al. 2012, and references therein) or further out (Yong et al. 2012; Donor et al. 2020) - or even more complicated functions (see e.g. Chiappini et al. 2001; Kubryk et al. 2015)?
- Different samples yield varying gradients, potentially due to biases in data or the inclusion of older stars (e.g. Boeche et al. 2013; Allende Prieto et al. 2006; Katz et al. 2011; Hayden et al. 2014; Anders et al. 2014; Vickers et al. 2021; Willett et al. 2023).
- The impact of spiral arm structures (Poggio et al. 2021), the Galactic warp (Lemasle et al. 2022) or bar-driven mixing (Di Matteo et al. 2013) on metallicity gradients is not fully understood.
- Methodologies for fitting linear models to scattered data need re-evaluation (Metha et al. 2021).

Understanding these gradients in the Milky Way is also crucial for extragalactic studies, where spatial resolution limits observations. New instruments like the MUSE integral field spectrograph have enabled a plethora of extragalactic studies to contrast the Milky Way to and techniques like the spectroscopy of HII regions and planetary nebulae have helped to infer gas metallicity distributions in external galaxies (Shaver et al. 1983; Vilchez & Esteban 1996; Rolleston et al. 2000; Bresolin et al. 2012). Recent examples include Sánchez et al. (2014) with CALIFA galaxy observations as well as Mun et al. (2024) and Chen et al. (2024) who use MAGPI galaxy observations to probe for example the effects of spiral arms. Notable is also the scatter that Chen et al. (2023) found for the gas metallicity across galactic radius with TYPHOON observations (see their. Figs. 4-6). Grasha et al. (2022) found that the gas metallicity gradient plateaus at a lower limit in their TYPHOON galaxies at the outermost radii - an observation replicated by IllustrisTNG simulations (Hemler et al. 2021; Garcia et al. 2023).

From a modelling perspective, galactic chemical evolution models can both test understanding of radial metallicity gradients and make predictions beyond the limited volumes and tracers tested by Milky Way and extragalactic studies. Such galactic chemical evolution models include Chiappini et al. (2001); Matteucci (2001); Minchev et al. (2014); Kubryk et al. (2015); Stanghellini et al. (2015); Rybizki et al. (2017). Sharda et al. (2021) even presented a model for gas phase metallicity gradients in galaxies and their evolution from first principles.

While Pilkington et al. (2012) found that such gradients are established by inside-out formation in RaDES simulations, whereas Tissera et al. (2019) used EAGLE simulations to study gradients across different galaxy characteristics, such as mergers and stellar mass. Bellardini et al. (2021) and Bellardini et al. (2022); Graf et al. (2024) compared the radial metallicity gradient and its azimuthal scatter for different simulations of the FIRE suite for gas and stars, respectively. Focusing on the change of the radial metallicity gradient over time, Grand et al. (2015) assessed the scatter of radial metallicity distribution for different stellar ages. Grand et al. (2016) looked at stars with ages below 3 Gyr in AURIGA and linked deviations from a global gradient towards slightly lower and higher metallicities with the leading and trailing edges of spiral arms, respectively. Grand et al. (2016) even found significant changes to the metallicity induced during 120 Myr, or roughly one galactic rotation. Both Ma et al. (2017b, see their Fig. 6) with FIRE and Agertz et al. (see their Fig. 9 2021) with VINTERGATAN further assessed the evolution of the radial metallicity gradient for gas and stars. Buck et al. (2023) studied how the gas metallicity gradient changes over time in the NIHAO-UHD simulations and found periods of time where the gradient surprisingly steepens. This finding resembles closely the findings of Lu et al. (2022) and Ratcliffe et al. (2023) for the Milky Way. This steepening phase could be connected and explained by major accretion events in the simulations. Khoperskov et al. (2023) again focused on the gas and found the scatter of the gas metallicity of $\approx 0.04-0.06$ dex at a given galactocentric distance.

This study here aims to advance these theoretical insight by addressing four critical scientific questions using a high-resolution simulation of a Milky Way analogue galaxy focusing on the inner $R_{\mathrm{Gal.}} \leq 20$ kpc:

(i) *Linearity of the gradient:* Assess the extent to which the radial metallicity gradient of young stars is linear.

(ii) *Scatter in the gradient:* Quantify the expected scatter in the radial metallicity gradient of young stars.

(iii) *Coherence of the gradient with position:* Investigate the gradient's variation with radial coverage and azimuth.

(iv) *Coherence of the gradient with age:* Determine the reliability of stars as tracers of the gas disk over different ages.

The paper is structured as follows: Section 2 describes the data of our Milky Way analogue NIHAO-UHD simulation. Section 3 analyses the linearity of the radial metallicity gradient of the simulation, the first of our four objectives. Section 4 then analyses both the scatter and local deviations from the gradient as well as the coherence of the gradient with vertical and azimuthal position as well as age (the remaining three objectives). Section 5 discusses them individually. We note that in this research we are mainly interested in the specific shape of the radial metallicity gradient for radii relevant to Galactic observations. However, we also discuss our results in the context of extragalactic results that probe beyond the inner 20 kpc of a galaxy. Section 6 bundles our results into an overarching conclusion.

2 DATA: A NIHAO-UHD MILKY WAY ANALOGUE SIMULATION

For this project, we use a cosmological zoom-in simulation of a Milky Way analogue (`g8.26e11`) from the *Numerical Investigation of a Hundred Astronomical Objects* (NIHAO, Wang et al. 2015) project. For this project, we limit the simulation data to the main halo by applying PYNBODY's implementation of the Amiga Halo Finder (Knollmann & Knebe 2009) and then reposition and rotate this main halo to be face-on based on the angular momentum with PYNBODY's ANALYSIS.ANGMOM.FACEON module (Pontzen et al. 2013). We then further transform the resulting galactocentric Cartesian coordinate (X, Y, Z) and velocities (V_X, V_Y, V_Z) to Cylindrical ones as done in a previous study of this main halo by Buder et al. (2024).

The model galaxy has a virial radius of $R_mathrmvir = R_{200} =$ 206 kpc and a total mass (gas, stars and dark matter) inside R_{vir} of $9.1 \cdot 10^{11}\,\mathrm{M}_\odot$. At redshift zero, it contains $8.2 \cdot 10^{11}\,\mathrm{M}_\odot$ dark matter, $6.4 \cdot 10^{10}\,\mathrm{M}_\odot$ gas mass and $2.3 \cdot 10^{10}\,\mathrm{M}_\odot$ stellar mass with a stellar mass resolution of around $7.5 \cdot 10^3\,\mathrm{M}_\odot$. When using a fifth of the virial radius as reference to calculate total luminosity[1] and mass, we estimate a half-light, that is, effective radius of $R_e = 3.79$ kpc and a half-stellar-mass radius of 2.97 kpc. This model galaxy was calculated as part of the NIHAO-UHD project (Buck et al. 2020) and has previously been used in various works studying Milky Way satellites (Buck et al. 2019), Milky Way's dark halo spin (Obreja et al. 2022) or inferring birth properties of stars with abundance clustering (Ratcliffe et al. 2022).

Simulations were carried out with the smoothed particle hydrodynamics code `Gasoline2` (Wadsley et al. 2017) using cosmological parameters from Planck Collaboration et al. (2014) with initial conditions and energetic feedback descriptions from the NIHAO project (Wang et al. 2015). Zoom-in simulations were then performed as described in detail by Buck et al. (2021) with star formation following Stinson et al. (2006) and energetic feedback following Stinson et al. (2013). We note that this is a slightly different rerun of the same simulation than the one studied by Buder et al. (2024). Here we are dealing with a higher resolution version and updated chemical yields.

Because computational resources still limit the mass resolution of simulations, we are relying on tracer particles that represent simple stellar populations (SSPs) with the same age, overall metallicity and discrete initial mass function (IMF). Buck et al. (2021) have implemented the flexible chemical evolution code CHEMPY (Rybizki et al. 2017) to calculate the chemical yields for the SSPs. In particular, we use the alternative (`alt`) setup of CHEMPY that assumes a Chabrier (2003) IMF with high-mass slope of $\alpha_{\text{IMF}} = -2.3$ over a mass range of $0.1 - 100\,\mathrm{M}_\odot$ for SSPs across a metallicity range of $Z/Z_\odot \in [10^{-5}, 2]$. The code calculates the contribution from asymptotic giant branch (AGB) stars, CCSN across a mass range of $8 - 40\,\mathrm{M}_\odot$, and SNIa with a an exponential function with exponent -1.12, a delay time of 40 Myr, and a normalization of the SNI rate of -2.9. For each of these nucleosynthetic channels, yields from the following studies are used: Chieffi & Limongi (2004) for CCSN, Seitenzahl et al. (2013) for SNIa, and Karakas & Lugaro (2016) for AGB stars (`new_fit` model in Buck et al. 2021). Contrary to a previous study by Buder et al. (2024), we take the elemental abundances at face value and do not apply any shifts.

To achieve a roughly similar selection as the observational data of the Milky Way (Genovali et al. 2014) and other galaxies (e.g. Chen et al. 2023), we restrict the simulation data to a galactocentric radius of $R_{\text{Gal}} \leq 20$ kpc, as shown in Fig. 1. Similar to the Milky Way (Poggio et al. 2018; Lemasle et al. 2022), we note a warp of the stellar and gaseous disk (see Figs. 1b and 1e, respectively).

To avoid too strong effects of radial migration (Binney & Tremaine 2008; Frankel et al. 2018; Grand et al. 2016; Minchev et al. 2018) while maintaining a sufficiently large sample size we further enforce stars to be younger than 0.5 Gyr, corresponding to roughly the time of four galactic rotations, and being half the value found by Minchev et al. (2018) for very limited migration in the Milky Way. This selection de-facto limits the vertical range of 99% of stars to $|z| = 1.4$ kpc. The strong influence of this age cut on the vertical distribution of stars in the Milky Way analogue can best be appreciated from the difference of vertical density distributions of stars in Figs. 1b and 1c. We are applying these cuts for all following analyses of the radial metallicity gradient in Section 3.

3 THE LINEARITY OF THE RADIAL METALLICITY GRADIENT IN NIHAO-UHD

In this section, we analyse the functional shape of the radial metallicity gradient. To get a first impression of possible shapes, we show the logarithmic density distribution of star particle iron abundances [Fe/H] across different galactocentric radii $R_{\text{Gal.}}$ in Fig. 2a. This distribution strongly suggests that the gradient is predominantly linear, similar to findings for the Milky Way. More complex shapes, such as piecewise linear ones have been suggested based on incomplete and limited data in the literature. We are thus also analysing these shapes with the complete and better sampled data points of the NIHAO-UHD simulation. We firstly test different global fits in Section 3.1, before testing the influence of binning and coverage in Sections 3.2 and 3.3, respectively.

3.1 Global gradient fits

We fit three different functional forms to the global data of Fig. 2, that is, a linear function, a piecewise linear with a break radius, and a quadratic function. The coefficients of the functions as fitted with the SCIPY.OPTIMIZE function CURVE_FIT (Virtanen et al. 2020) are listed in Table 1. To estimate the uncertainty of the break radius R_{break}, we use the profile likelihood method to identify the radii at which the RSS values are increased by 1σ from the best RSS radius in steps of $\Delta R_{\text{break}} = 0.1$ kpc and 0.5 kpc for the full and binned data

[1] Using PB.ANALYSIS.LUMINOSITY.HALO_LUM (Pontzen et al. 2013).

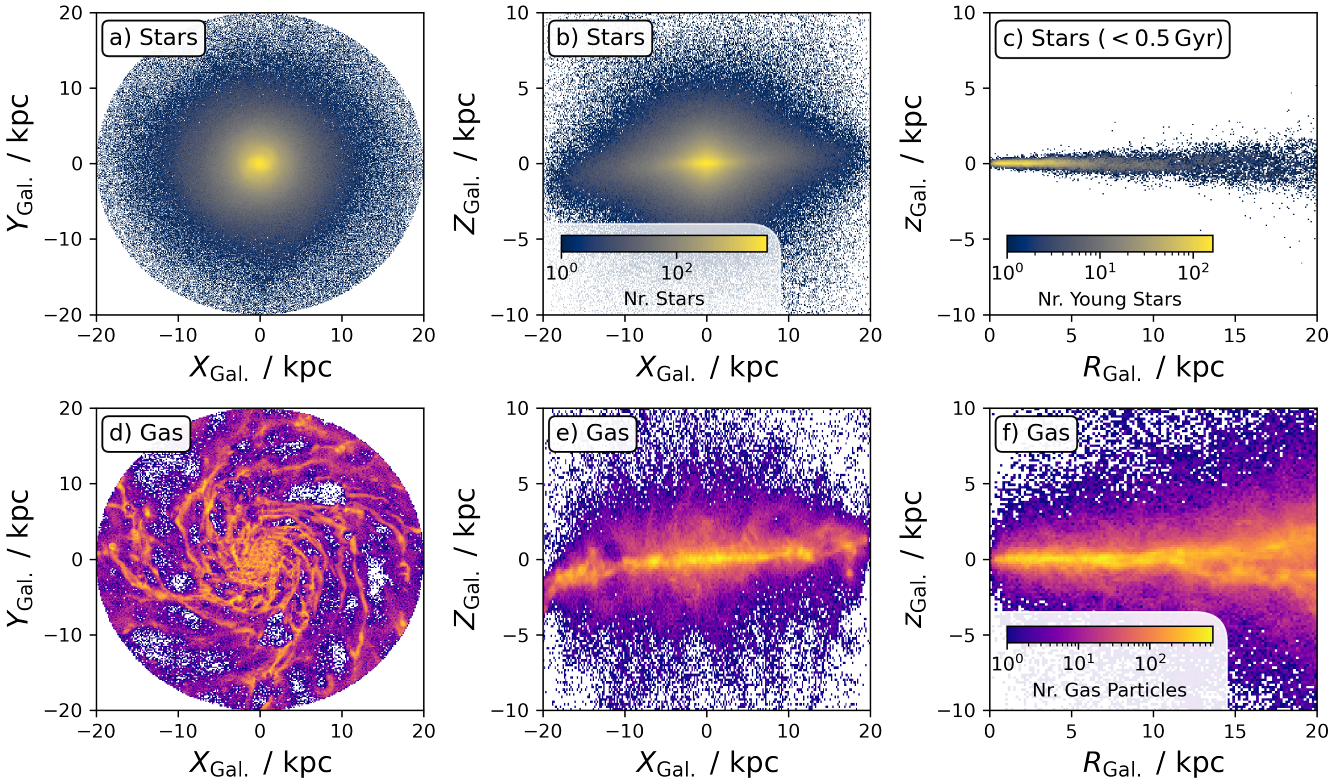

Figure 1. Logarithmic spatial density distribution of stars (upper panels) and gas (lower panels) within $R < 20$ kpc $\sim 5\,\mathrm{R_e}$ of the NIHAO-UHD Milky Way analogue `g8.26e11` in galactocentric cartesian and cylindrical coordinates. Panel c) shows the influence of selecting only young stars with ages below 0.5 Gyr.

set, respectively. We have confirmed the robustness of our fits by applying other fitting routines as outlined in Appendix A.

Having fitted three different models, will use a combination of parameters to judge which model fits better. Firstly, we are computing the residual sum of squares (RSS) as

$$RSS = \sum_i^n \left([\mathrm{Fe/H}] - g(R_{\mathrm{Gal.}})\right)^2 . \tag{2}$$

We see from Table 1 that this value is smallest (although only by a small margin) for the quadratic function. When assuming $\sigma^2 = RSS/n$, we can then define a logarithmic likelihood

$$\ln L = -\frac{n}{2}\ln(2\pi) - \frac{n}{2}\ln\frac{RSS}{n} - \frac{n}{2} \tag{3}$$

for our n data points. For k free parameters, we can then calculate the Akaike Information Criterion (AIC) and the Bayesian Information Criterion (BIC) as

$$AIC = 2k - 2\ln L \qquad BIC = k\ln n - 2\ln L. \tag{4}$$

Again, the quadratic function performs slightly better than the linear or piecewise linear functions (see Table 1).

We show the fit residuals in Fig. 2b as density distribution as well as in Fig. 2c as percentile distributions in radial bins of $\Delta R_{\mathrm{Gal}} = 0.5$ kpc. While the density distribution shows a lot of substructure, that we are investigating later in Section 4, we note an increase of the median residuals of the linear fit in Fig. 2c towards inner and outer radii, especially for $R_{\mathrm{Gal.}} > 17$ kpc. A quadratic fit (see orange lines in Fig. 2) results in a slightly steeper linear component of the gradient (from -0.0411 to $-0.0497\,\mathrm{dex\,kpc^{-1}}$), which is counteracted by the quadratic flattening term of $+0.0005\,\mathrm{dex\,kpc^{-2}}$. The latter leads to an effective flattening of $-0.172 + 0.200 = 0.028$ dex (linear vs. quadratic terms) at $R_{\mathrm{Gal.}} = 20$ dex. While seemingly only a nuisance correction across the large extend of [Fe/H] and $R_{\mathrm{Gal.}}$, this quadratic function is evidently superior to the linear fit. This can be best appreciated in Fig. 2c, where the orange line is tracing the median residuals from the linear function much better across all the radii. This suggests a non-linear such as a piecewise linear or quadratic form to the gradient.

Discerning between the latter functional forms proves difficult. All fitting quantitative fitting performance indicators of RSS, AIC, and BIC have very similar values between the two forms and when zooming into the residuals of the different shapes in Fig. 3, we see no visual advantage of either form.

Take-Away: Piecewise linear and quadratic functions perform both better than a linear fit to the radial metallicity relation. However, we see no significant preference between piecewise and quadratic functions based on our assessments.

3.2 The influence of binning

In this section, we test the influence of fitting a function to all points of the distribution or to binned data in steps of $\Delta R_{\mathrm{Gal.}} = 0.5$ kpc, using mean values as data points and standard deviations[2] as uncertainty

[2] We note that this σ is not equivalent to an observational uncertainty and can thus not be directly applied onto observational analyses.

Table 1. Fit Evaluation of linear, quadratic, and piecewise linear fits. Extra parameters are quadratic term and break radius for the quadratic and piecewise fit. RSS stands for Residual Sum of Squares (Eq. 2). AIC stands for Akaike Information Criterion and BIC stands for Bayesian Information Criterion (see Eq. 4).

Function	Intercept ($a_0 \pm \sigma_{a_0}$)	Slope ($a_1 \pm \sigma_{a_1}$)	Extra Parameter	RSS	AIC	BIC
Linear	0.46266 ± 0.00039	-0.04109 ± 0.00005	–	87.0	-118270	-118260
Quadratic	0.48031 ± 0.00055	-0.04864 ± 0.00018	0.00045 ± 0.00001	82.7	-120150	-120120
Piecewise	-0.04477 ± 0.00010	0.47473 ± 0.00047	–	82.9	-120090	-120050
	–	-0.03562 ± 0.00014	9.3 ± 0.1			
Linear (bins)	0.46849 ± 0.00567	-0.04169 ± 0.00127	–	0.0147	-200	-200
Quadratic (bins)	0.47327 ± 0.00674	-0.04611 ± 0.00359	0.00031 ± 0.00024	0.0033	-260	-250
Piecewise (bins)	-0.04398 ± 0.00207	0.47190 ± 0.00617	–	0.0026	-260	-260
	–	-0.03547 ± 0.00461	10.0 ± 0.5			

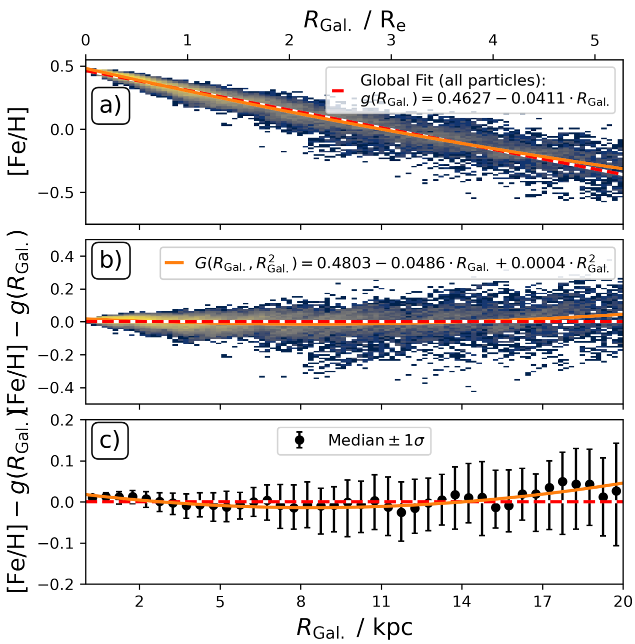

Figure 2. Global fits and deviation to the radial metallicity gradient R – [Fe/H]. Functional forms of the linear (red) and quadratic (orange) lines are shown in the legend. Panel a) shows the underlying data of all data points as logarithmic density and the global fit to them as red dashed line. Panel b) shows the deviation of data from a linear gradient as logarithmic density plot, whereas panel c) shows the 16th and 84th percentile around the median deviation as error bars in $\Delta R_{\mathrm{Gal}} = 0.5$ kpc bins.

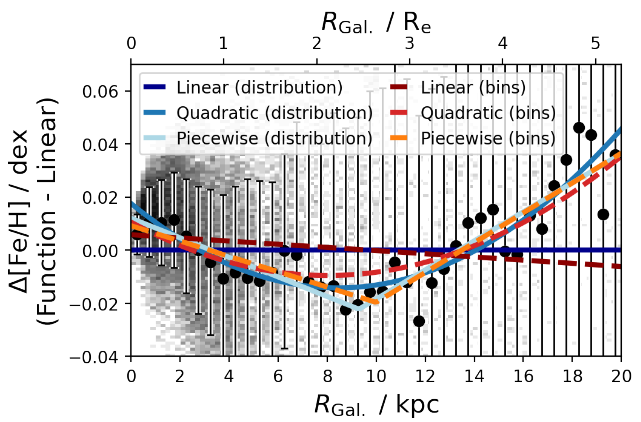

Figure 3. Same as Fig. 2c, but overplotting the different functions (linear, quadratic, and piecewise linear) estimated from the full distribution (solid lines) or from means and standard deviations (error bars) in $\Delta R_{\mathrm{Gal.}} = 0.5$ kpc bins (dashed lines).

(see also Hemler et al. 2021, who fitted functions to radially binned IllustrisTNG data). Our results are plotted in Fig. 3. Given that more than half of the young star particles of the galaxy are within $R_{\mathrm{Gal.}} < 4$ kpc, this binning - although counteracted by the smaller spread of [Fe/H] in the inner galaxy - is weighing the distribution of inner galaxy significantly less then when weighing all particles equally (20 vs. 34 000 data points). The fitted parameters to binned data exhibit a larger uncertainty due to our use of the spread of [Fe/H] per bin as absolute uncertainty σ, but the fitted parameters are agreeing well and truly within the fitting uncertainties.

Take-Away: While the specific slopes differ when fitting all points or binned data, they agree within the still rather small fitting uncertainties.

3.3 The influence of radial coverage on linear fits

While we have gained a useful insight into the global function, observational data will rarely cover the full extend of the stellar disk. Milky Way studies have previously been limited to the range of around 5 – 15 kpc. There are often similar limitations and even gaps in extragalactic data. Using smaller ranges, observational studies have found hints of piece-wise linear gradients with a break radius in them based on a limited radial coverage (e.g. Andrievsky et al. 2002a; Yong et al. 2012; Boeche et al. 2013; Hayden et al. 2014; Anders et al. 2017; Donor et al. 2020; Chen et al. 2023). These results are intriguing, since a quadratic function can to first order be approximated by two linear functions with a break radius. We therefore want to use this simulation to test if the radial coverage may indeed delude us into identifying broken linear gradients.

In Fig. 4, we test how smaller coverage and piecewise linear fits could mimic a complex global gradient. We test fits across piecewise linear radial ranges of 0.25, 0.5, 1, 2, 5, 8, 10, 15, and 20 kpc. We show their difference with respect to a global linear fit in Fig. 4, with color-coding indicating the local gradient slope. In this figure, a horizontal dashed line indicates the same slope as the global fit, whereas the offset of a line from said horizontal dashed line indicates the local deviation from the global gradient intercept. Differences in line slopes are visualising the difference in gradient slopes between the global and local fits. We see that all ranges are suggesting more or less significant deviations from a global linear fit. The innermost fit is suggesting a significantly different gradient than the outermost fit. We also note increasing slope differences towards the smallest

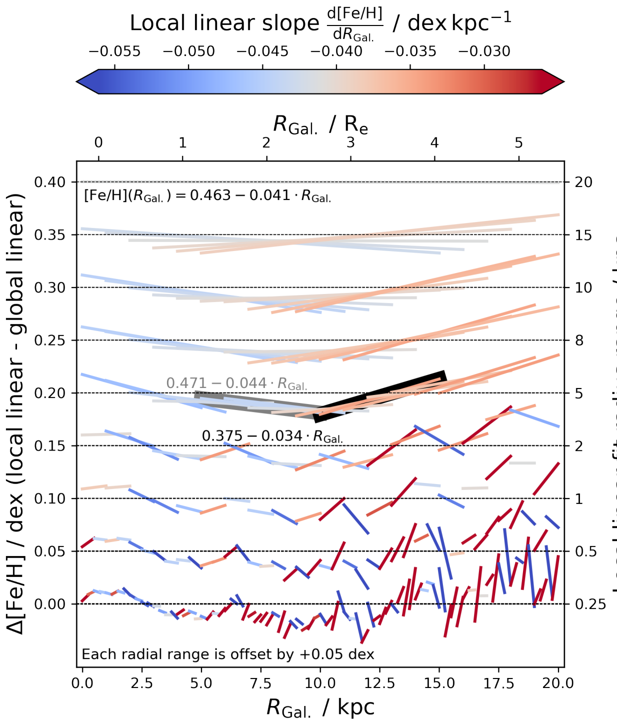

Figure 4. Impact of different coverage in galactocentric radius when fitting a linear radial metallicity gradient to young stars. Each horizontal segment is using a different running radial fitting range between 0.25 and 15 kpc as outlined on the right. For better contrast, the global linear fit is subtracted from the local gradient estimates and each line is colored by the gradient slope with a color scale centered around the global fit slope. Additionally, the slope of each line segment highlights the difference between global and local slope. This means, if the local fit exactly matches the global fit, we display it as a flat line (zero slope difference) on top of the gray dashed line (zero offset deviation) and give it a gray color signaling the same gradient value as the global fit.

scales, hinting at local deviations from a global pattern. We follow these up in Section 4, but for now focus on the larger-scale trends.

When directly comparing an inner and outer radius fit, such as between $R_{\mathrm{Gal.}} = 5 - 10\,\mathrm{kpc}$ (thick grey line in Fig. 4) and $R_{\mathrm{Gal.}} = 10 - 15\,\mathrm{kpc}$ (thick black line in Fig. 4), we note a significant change, similar to previous estimates of the Milky Way (e.g. Yong et al. 2012; Lemasle et al. 2008). In our case the gradient estimate changes from $\mathrm{[Fe/H]}(R_{\mathrm{Gal.}}) = 0.471 - 0.044 \cdot R_{\mathrm{Gal.}}$ to $\mathrm{[Fe/H]}(R_{\mathrm{Gal.}}) = 0.375 - 0.034 \cdot R_{\mathrm{Gal.}}$. When looking at linear gradient fits across radial coverage of $\Delta R_{\mathrm{Gal.}} = 5 - 15\,\mathrm{kpc}$ in Fig. 4, the gradient was steeper (bluer color) for smaller radii and flatter (redder) for larger radii. Indeed, a piecewise linear function can well mimic a complex global gradient.

We note that in the simulated data, we see local deviations becoming traceable below $\Delta R_{\mathrm{Gal.}} \leq 2\,\mathrm{kpc} \sim 0.5\,\mathrm{R_e}$ (bottom part of Fig. 4). This might indicate the necessary spatial resolution to see local effects, such as spiral arms, for extragalactic studies. We pursue this observation in the following Section 4.

Take-Away: We find that a piecewise linear function can well mimic a quadratic function across the scales used in Milky Way and extragalactic studies. Local deviations become traceable below are spatial resolution of $\Delta R_{\mathrm{Gal.}} \leq 2\,\mathrm{kpc} \sim 0.5\,\mathrm{R_e}$.

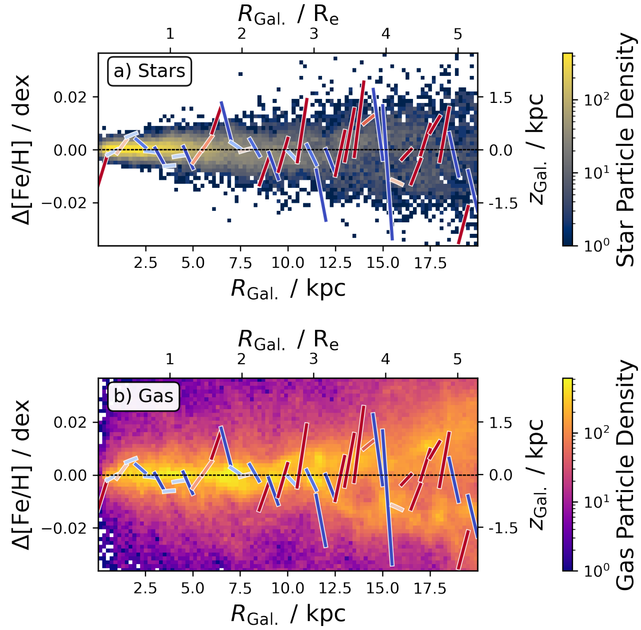

Figure 5. Local gradient deviations similar to the second lowest row of Fig. 4 for radial gradients in 0.5 kpc steps (but compared to a global quadratic function) overlapped on top of the logarithmic density distribution in $R - z$ for $|z| < 3\,\mathrm{kpc}$ of gas (panel a) and stars (panel b).

4 SCATTER AND LOCAL DEVIATIONS FROM THE GRADIENT

Now that we are sufficiently satisfied that our flattening gradient function reproduces the overall shape of the radial metallicity gradient, we are concerned with both the scatter and local slope deviations across the galactocentric radii in this section. In detail, we analyse the scatter (Section 4.2), vertical and azimuthal variations (Sections 4.2 and 4.3, respectively) as well as deviations across different ages (Section 4.4).

4.1 Scatter

When investigating the change of scatter from the innermost radii to the outermost (see Fig. 2c), we see a steady increase in $1 - \sigma$ spread. This spread increases from

$\sigma\mathrm{[Fe/H]} = 0.01\,\mathrm{dex}$ at $R_{\mathrm{Gal.}} = 0.25 \pm 0.25\,\mathrm{kpc}$ to
$\sigma\mathrm{[Fe/H]} = 0.06\,\mathrm{dex}$ at $R_{\mathrm{Gal.}} = 8.25 \pm 0.25\,\mathrm{kpc}$ and finally reaches
$\sigma\mathrm{[Fe/H]} = 0.1\,\mathrm{dex}$ at $R_{\mathrm{Gal.}} = 19.75 \pm 0.25\,\mathrm{kpc}$, the largest $R_{\mathrm{Gal.}}$.

When reminding ourselves of the observed significant spread in metallicities of young open cluster at the solar radius beyond observational uncertainty (e.g. Donor et al. 2020; Spina et al. 2021) and our selection of only young (<0.5 Gyr) stars from the simulation, a strong impact of this scatter by radial migration should be excluded. At this point, we can imagine that this chemical diversity might be caused by less well mixed gas or non-radial effects (such as vertical or azimuthal ones), which we investigate subsequently.

4.2 Vertical deviations

In this section, we are now looking into deviations with respect to the vertical dimension, that is, $R - z$. In Fig. 5 we are showing the previously identified local gradient deviations (lines following the left

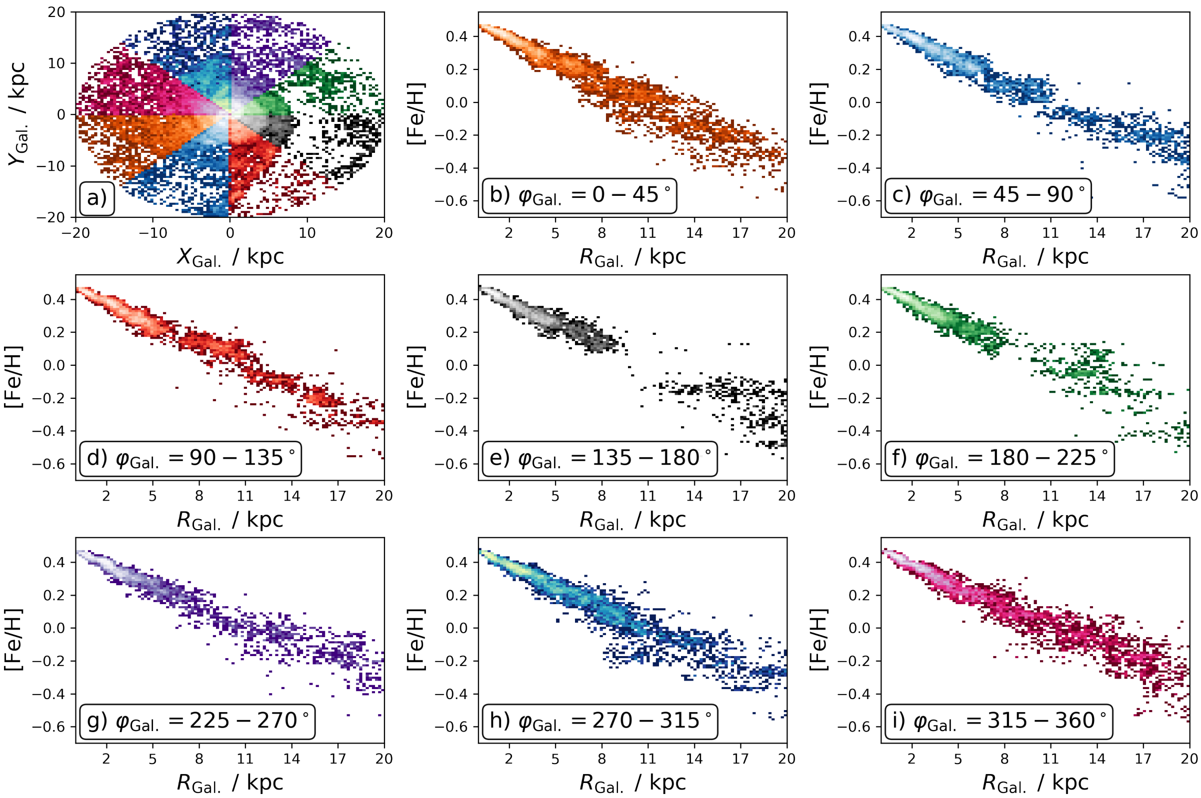

Figure 6. Stellar density variation across 8 different sectors (with color-code visualised in panel a) of the radial metallicity gradient $R-[\mathrm{Fe/H}]$ across 8 different azimuth ranges (panels b-i). A rotating lighthouse-like GIF animation of the median age and median density of the $R-[\mathrm{Fe/H}]$-relation across different azimuths is freely available on a repository.

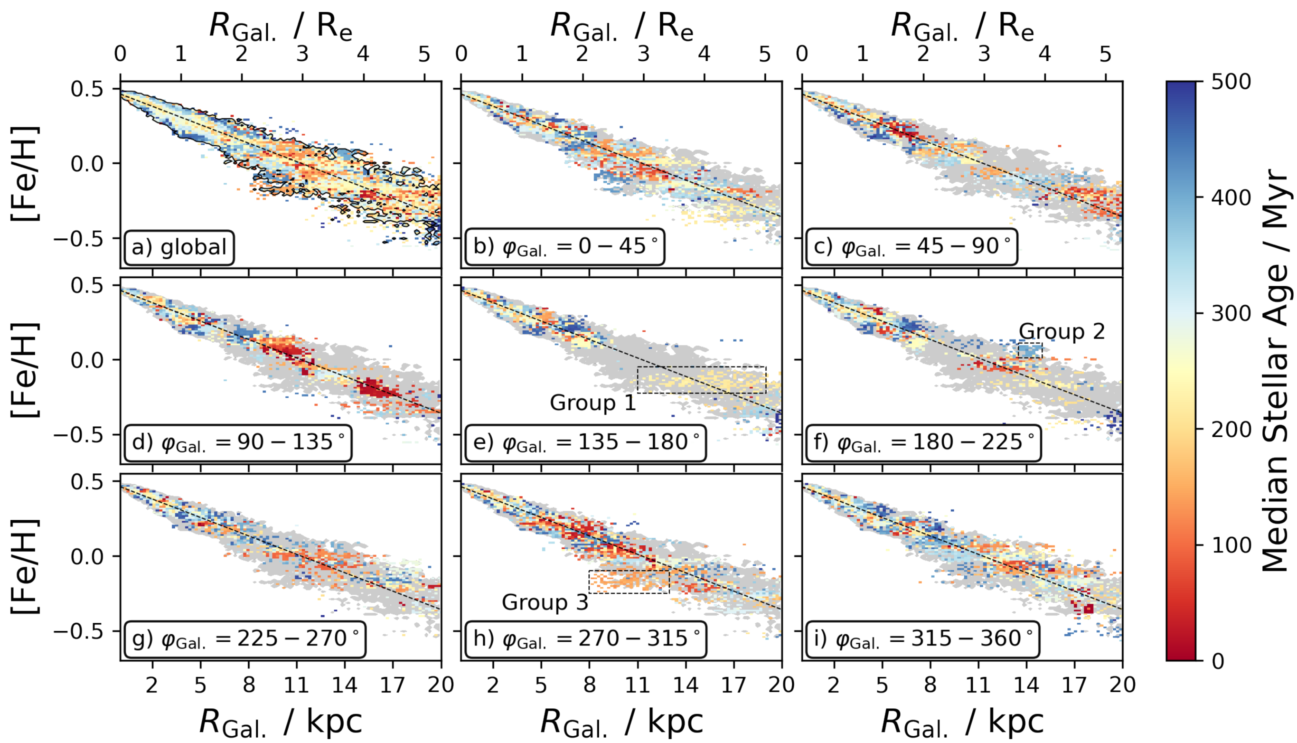

Figure 7. Same as Fig. 6, but colored by median age per bin. We identify 3 A rotating lighthouse-like GIF animation of the median age and median density of the $R-[\mathrm{Fe/H}]$-relation across different azimuths is freely available a repository.

axis label) on top of the vertical density distribution ($R - z$) of gas (Fig. 5a) and young stars (Fig. 5b) between $-3 < z < 3$ kpc. While the quickly decreasing amount of young stars (Fig. 5b) at outer radii does not show substructure in the density plots for reasonable bin sizes, we see more substructure for the gaseous component in Fig. 5a). In particular, we see rather minor deviations at small radii (where most stars and gas are close to the plane). At increasing radii, we notice an increase in both the vertical distribution of stars, as well as increasing local gradient deviations. In particular, we note a significant deviation of the slope around $R_{\mathrm{Gal.}} \sim 15$ kpc, where the gradient deviation line is steep and blue (indicating a much steeper gradient at this radius), and we notice a significant overdensity of gas around $z \sim 1$ kpc. Overall, however, we do not see strong correlations in this particular plane. This could, however, be caused by a super-position effect of the up- and downturn at larger radii due to the galactic warp (see Fig. 1e). We note that the superposition in Fig. 5c could smear out local correlations of slope changes with gas overdensities, for example, by spiral arms.

While such an edge-on view of the galaxy may indeed be the only observable one for extra-galactic targets, for example of the GECKOS survey of edge-on galaxies (van de Sande et al. 2023), we have the luxury of being able to analyse the azimuthal direction of our simulated galaxy, too. This seems especially important, as we have seen a significant warping of the gaseous and stellar disk of our simulated galaxy (see Figs. 1b and 1e). While the warp of the stellar disk in Fig. 1b is not as clear, we confirm that both the gas disk and the youngest stars below 0.5 Gyr are tracing each other across the simulation in both galactocentric radius $R_{\mathrm{Gal.}}$ and height $z_{\mathrm{Gal.}}$ for different sectors in azimuthal direction.

Take-Away: We see no strong correlations of deviations in the vertical direction across the whole simulation. Such correlations could, however, be blurred by azimuthal effects, like the galactic warp, which needs to be disentangled in the azimuthal dimension.

4.3 Azimuthal deviations

To analyse the deviations from a global gradient across different azimuthal viewing angles, we divide the galaxy into 8 sectors with $\Delta\varpi_{\mathrm{Gal.}} = 45$ deg (see Fig. 6a). This allows us to study the positions around the upturn and downturn of the galactic warp with the median azimuth of young star particles below and above the plane being $\varphi_{\mathrm{Gal.}} \sim 183$ deg and $\varphi_{\mathrm{Gal.}} \sim 4$ deg, respectively (see Fig. 1e), while maintaining a reasonable sample size.

At face value, the distribution of $R_{\mathrm{Gal.}}$ – [Fe/H] for each sector follows a similar, rather linear shape with most stars being born in the inner 5 kpc of the galaxy. However, we find significant deviations in different sectors of the galaxy (Fig. 6). One the one hand, we find non-linear deviations as bumps with slightly increased or decreased iron abundance - up to $0.1 - 0.2$ dex - in Figs. 6c at $R_{\mathrm{Gal}} \sim 18$ kpc, 6d at $R_{\mathrm{Gal}} \sim 10$ kpc, 6f at $R_{\mathrm{Gal}} \sim 14$ kpc, and 6g at $R_{\mathrm{Gal}} \sim 17$ kpc. On the other hand, we find significant gaps in the distribution at similar [Fe/H], most strikingly at the upturn of the galactic warp in Fig. 6e ($\varpi_{\mathrm{Gal.}} = 135 - 180\,°$) at [Fe/H] ~ 0 dex and $R_{\mathrm{Gal.}} \sim 8 - 14$ kpc. We note that the sector (e) with a gap is surrounded by two sectors with significant overabundance at the same radius (d and f). This could be indicative of gas from this particular region having moved towards either of azimuthal direction, causing a gas overdensity which could in turn lead to higher star formation activity. To establish this observation, we take a closer look at the time-domain, that is, stellar age as well as the spatial domain of $R_{\mathrm{Gal.}} - \varphi_{\mathrm{Gal.}}$ in the next section.

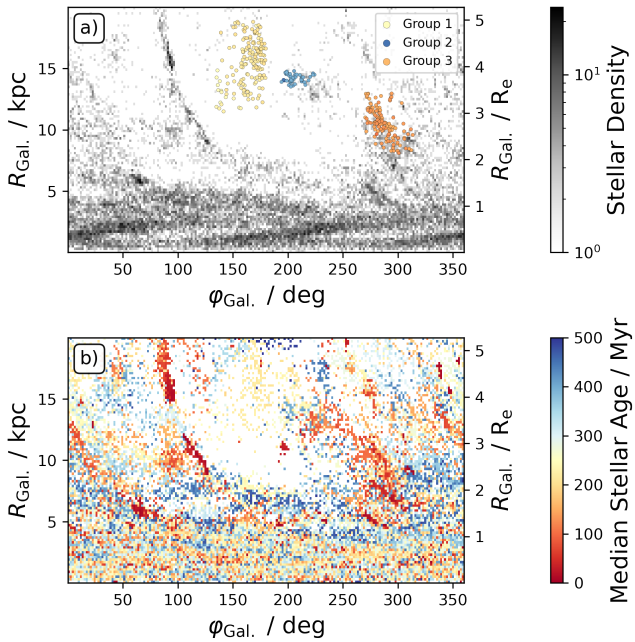

Figure 8. Density distribution (panel a) and age distribution (panel b) of young stars in the azimuthal and radial direction $\varphi_{\mathrm{Gal.}} - R_{\mathrm{Gal.}}$. In panel a), we also show the groups previously identified in Fig. 7.

Take-Away: We find various deviations from the global trend in azimuthal direction, including gaps as well as isolated streaks of stars with similar [Fe/H] across $\Delta R_{\mathrm{Gal.}} = 2 - 6$ kpc. These can introduce local over- and under-enhancement of up to ± 0.2 dex in [Fe/H] at a given radius. In the next section, we analyse if the stars of these streaks have been born at the same or different time.

4.4 Deviations with time and age

In this section, we look at the radial metallicity gradient across a small age range of less than 0.5 Gyr. To do so, we color Fig. 6 by median stellar age rather than logarithmic density in Fig. 7. We find an overall significant scatter across time, suggesting a good mix of star formation across all sectors for stars born within less than 0.5 Gyr. For stars within this restricted age range, we do not see a strong correlation with radius, such as older stars being born further inside, but clearly a larger amount of stars being born closer to the galactic centre. We note that stars with similar [Fe/H] in each sector tend to be formed at similar times (within 50 Myr), that is, as flat lines with same color (age) in Figs. 7b-i. To guide the eye, we have an identified Group 1 in Fig. 7e (around $R_{\mathrm{Gal.}} \sim 14$ kpc at $\varpi_{\mathrm{Gal.}} = 180 - 225\,°$). We further note that the enriched bumps identified earlier are born at similar times, see for example Group 2 in Fig. 7f. The coloring by age also reveals that stars with lower [Fe/H] than expected (see Group 3 in Fig. 7h) are born at similar times. In some cases, these extend to $\Delta R_{\mathrm{Gal.}} = 2 - 6$ kpc, see Groups 1, 2, and 3 in Fig. 7. At a given radius $R_{\mathrm{Gal.}}$, these streaks are causing a significant spread in local [Fe/H] of up to ± 0.2 dex (see Fig. 7).

From the analysis of azimuthal sectors, the impression arose that the star formation in this simulated Milky Way analogue is - as expected for a spiral galaxy - rather patchy and localised on the smallest timescales. This is confirmed when looking at the spacial distribution of azimuth $\varphi_{\mathrm{Gal.}}$ and radius $R_{\mathrm{Gal.}}$ in Fig. 8. Already

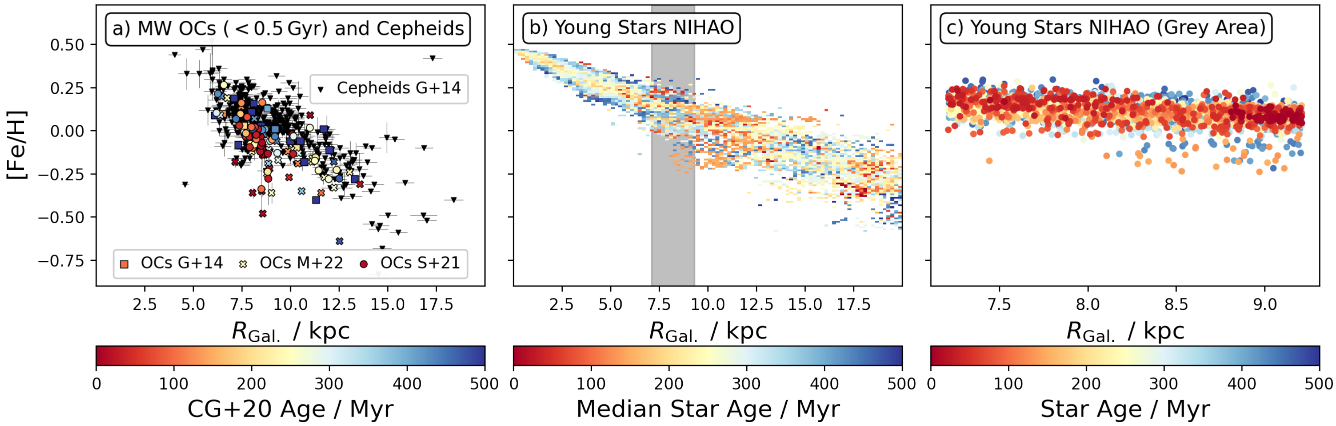

Figure 9. Comparison of the Milky Way's radial metallicity trend as traced by Cepheids (black triangles, compiled from literature by Genovali et al. 2014, G+14) as well as young (<0.5 Gyr) open cluster of the Milky Way as traced by the literature compilation from Genovali et al. (2014, G+14 as squares), APOGEE DR17 from Myers et al. (2022, M+22 as crosses), and GALAH DR3 from Spina et al. (2021, S+21 as circles). The latter two are compiled based on the membership and age catalogue by Cantat-Gaudin & Anders (2020, CG+20).

when looking at the density distribution of all stars born within less than 0.5 Gyrin Fig. 8a, multiple streams are visible - stars on spiral patterns (see also Kreckel et al. 2019, and Chen et al., submitted). When following up the previously identified Groups 1, 2, and 3, we recover them on said spiral patterns (Groups 1 and 3) or a local overdensity (Group 2). While one could imagine that radial migration might induce such a spiral-like shape for the stars of groups 1 and 3, their low age of less than 250 Myr would need a significant migration effect of several kpc, while not having an influence on the older stars of group 2. When tracing the position of significant overdensities from Fig. 8a in the same projection colored by age in Fig. 8b, we note that for radii above $R_{\mathrm{Gal.}} > 5$ kpc these overdensities are colored in red, that is, containing indeed young stars with ages below 200 Myr and being consistent with the most recent star formation along these spiral patterns in the outer galaxy.

Take-Away: We find significant scatter across the radial metallicity distribution caused by streaks of stars born with similar [Fe/H] at similar times (within 50 Myr) across either very local or radially extended spiral-shaped regions of the galaxy, suggesting local enhancement patterns in small overdensities or along spiral arms.

5 DISCUSSION

Having presented the analysis, we are now putting our results into the context of other work in terms of our initial aims, that is to analyse the shape (Section 5.1) scatter (Section 5.2), local deviations (Section 5.3), and time-dependence (Section 5.4) of the radial metallicity gradient. These initial discussions inform our thoughts on the implications of this work for Milky Way studies in Section 5.5 and the studies of other galaxies in Section 5.6.

5.1 Linearity of the radial metallicity gradient

The radial metallicity gradient of our simulated NIHAO-UHD Milky Way analogue showed an overall decreasing, predominantly linear shape, as established in Section 3. Motivated by the previous works by Sánchez-Menguiano et al. (2016), among others, we also fitted piecewise linear and quadratic functions to the data in Section 3.1. Both were clearly performing better than linear. Between them the very similar fitting performance indicator indicate no significant preference between either piecewise linear or quadratic function. We note that due to the rather good overall fit of both functions, we have not tried more exotic non-linear functions as done by Scarano & Lépine (2013). Increasing the flexibility of the gradient function could, however, improve the fit at the innermost kpc, where a flattening is predicted by our simulation, but chemical enrichment is also harder to simulate (see also Minchev et al. 2013). We have found no significant influence of binning for our gradient estimates (Section 3.2), but have found that a limited radial coverage - as is the case for the Milky Way - could mimic a truly quadratic function with two piecewise linear fits (Section 3.3). This is important, as it has significant implications for the conclusions we draw from the incomplete data of our Milky Way, as we will discuss in more detail in Section 5.5.

The balance between a quadratic and piecewise linear radial metallicity gradient teeters at the breaking radius. If present, our analysis of the Milky Way analogue would place it at $R_{\mathrm{break}} \sim 10 \pm 0.5$ kpc. This radius is strikingly close to the radius of 9 kpc found by Hemler et al. (2021) for a TNG50 galaxy simulation with a stellar mass of $\log(M_\star/\mathrm{M}_\odot) = 10.72$, that is, close to the Milky Way's (see their Fig. 2). In terms of physical reasons for a breaking radius at this location, a direct and secular influence of a stellar bar with non-symmetric effects around the corotation radius (Di Matteo et al. 2013; Scarano & Lépine 2013) should be minor for our specific scenario due to the low ages of the stars considered in our analysis. In particular, our identified break radius is significantly larger than the corotation radius of the Milky Way bar at 4.5 – 7.0 kpc (Bland-Hawthorn & Gerhard 2016, and references therein) anyway. We are intrigued, however, by the proposition by Garcia et al. (2023) of galactic discs consisting of a star-forming inner disc with a steep gradient and a mixing-dominated outer disc with a flat gradient, with the break radius marking the region of transition between them. In Illustris TNG50-1 data, they found such a transition and break radius to be situated much further out at 30 kpc for Milky Way mass galaxies ($10.1 \leq \log(M_\star/\mathrm{M}_\odot) \leq 10.6$). While our best-fitting break radius - if present - is inconsistent with theirs, we will follow this up in more detail in Section 5.6, where we also discuss the implications for extragalactic studies in general.

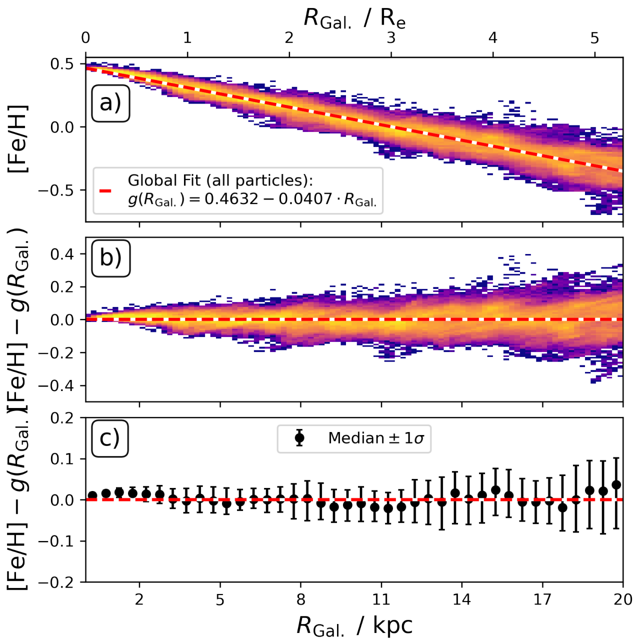

Figure 10. Same as Fig. 2, but for gas.

5.2 Scatter of the radial metallicity gradient

In Section 4.1 we found an increasing scatter from σ[Fe/H] = 0.01 dex in the inner galaxy to σ[Fe/H] = 0.1 dex around $R_{\mathrm{Gal.}} \sim$ 20 kpc. Comparing these values with simulations other than TNG50 with a similar metallicity spread (see Fig. 2 by Hemler et al. 2021) is rather difficult, as the literature focusses on the shape and density distribution (see e.g. Minchev et al. 2014, their Fig. 10). When comparing with Milky Way studies (e.g. Anders et al. 2017), the scatter in the simulation is smaller than the observed spread of [Fe/H]. This can be visually appreciated by comparing the combinations of different measurements in the Milky Way (Genovali et al. 2014; Spina et al. 2021; Myers et al. 2022) in Fig. 9a and our simulation in Fig. 9b and c. We discuss the implications of this on studies of the Milky Way's gradient in Section 5.5.

When assuming that young star and gas phase abundances are similar, we find comparable scatter of abundances for example with respect to TYPHOON observations by Chen et al. (2023). To test this assumption, we also show the gas phase metallicity in Fig. 10, for which we find a similar shape and scatter of the gradient, but systematically less scatter or spread than observed gas phase abundance, thus urging us to treat the absolute values of abundances and abundance scatters as well as spreads with caution. We furthermore note that the spread of abundance in observations does only increase for some but not all of the observed galaxies by Chen et al. (2023), thus potentially limiting the range of galaxies to which our conclusions may apply.

5.3 Localised vertical and azimuthal deviations and their correlation with gas

In Sections 4.2 and 4.3 we have established that local deviations contribute significantly to the spread of the global metallicity gradient above $R_{\mathrm{Gal.}} > 8$ kpc $\sim 2\,\mathrm{R_e}$. We noted in particular a void of stars where we found an upturning warp of the galaxy around $\varphi_{\mathrm{Gal.}} \sim$ 180 deg spatially close to regions of the galaxy (Groups 1 and 2) that deviated most significantly from the overall trend in Fig. 7 and Fig. 8.

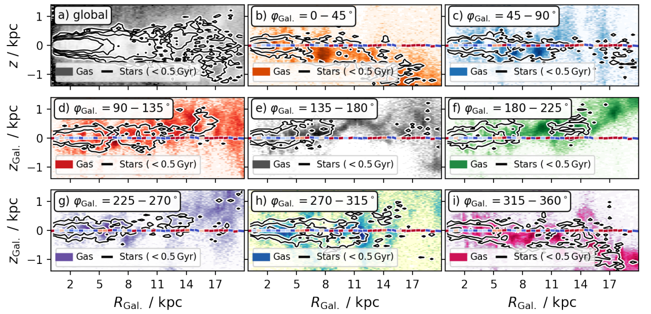

Figure 11. Tracing young stars and gas across galactocentric radii $R_{\mathrm{Gal.}}$ and height $z_{\mathrm{Gal.}}$ across the whole galaxy (panel a) and different azimuthal ranges/sectors (panels b-i). Small rectangles with cool-warm colors along the horizontal axis indicate the local gradient slopes as in Fig. 5.

These stellar voids pose the question if they are also void of gas thus suggesting the gas has shifted to the more enhanced regions. In Fig. 11 we are thus tracing both the spatial distribution of gas as colored density distribution and stars as grey contour lines and gas. We find that while stars and gas trace each other in the vertical direction, we do not always see a match between the two tracers in the radial direction. In particular, we do find a significant amount of gas around the stellar void of $\varphi_{\mathrm{Gal.}} \sim 180$ deg and $R_{\mathrm{Gal.}} \sim 8-11$ kpc in Figs. 11e and 11f. This gas seems to be more tightly concentrated though for example in the tight wave around $R_{\mathrm{Gal.}} \sim 8$–11 kpc in Fig. 11e. We also note that significant gas overdensities, for example around $\varphi_{\mathrm{Gal.}} \sim 0-45$ deg and $R_{\mathrm{Gal.}} \sim 7$ kpc in Fig. 11a do not seem to correlate with significant overenhancement in iron abundance (compare to Fig. 6a and Fig. C1). While we see a hint of a coinciding deviation of Δ[Fe/H] for larger deviations from the galactic plane Δz in the upturning outer region of Fig. 11f, this does not seem to be the case for the downturning outer region of Figs. 11b and 11i.

As the edge-on projection is not providing conclusive insights, we are now looking into the phase-on projection in Fig. 12. We have chosen a region of the simulated galaxy whose gas density at solar radius (Fig. 12c) matches with the recently measured distribution of young stars in the Milky Way at face value (Fig. 12a) by Poggio et al. (2021). Comparing simulated gas and observed young stars is preferable in this case, as the density of simulated stars is too low to easily identify overdensities (Fig. 12b). The region and its gas spiral structures appears to be representative, as these structures exist throughout the whole galaxy (see Fig. 1d).

In the different panels of Fig. 13, we thus showing this representative region of the galaxy, but color each spatial bin by stellar metallicity (13a) the deviation from the global linear trend (13b) as well as the gas metallicity (13c) and its deviation from the global linear trend (13d). In all cases, we also overlay the density contours of the significant gas overdensities (red regions in Fig. 12c). As expected, we see that the metallicity color map of the stars in Fig. 13a shows a decreasing trend from right to left (inner to outer galaxy) and an increasing scatter (more blue and red points towards the left) in the residual plot of Fig. 13b. We cannot identify a strong correlation of gas overdensities and metallicity or residuals in either plot - possibly caused by the low number density. In Figs. 13c and 13d, however, the radial gas metallicity gradient shows significant local variations, that is, a trend from left to right that is not very smooth. In particular, we find significant deviations of up to +0.15 dex in [Fe/H] behind

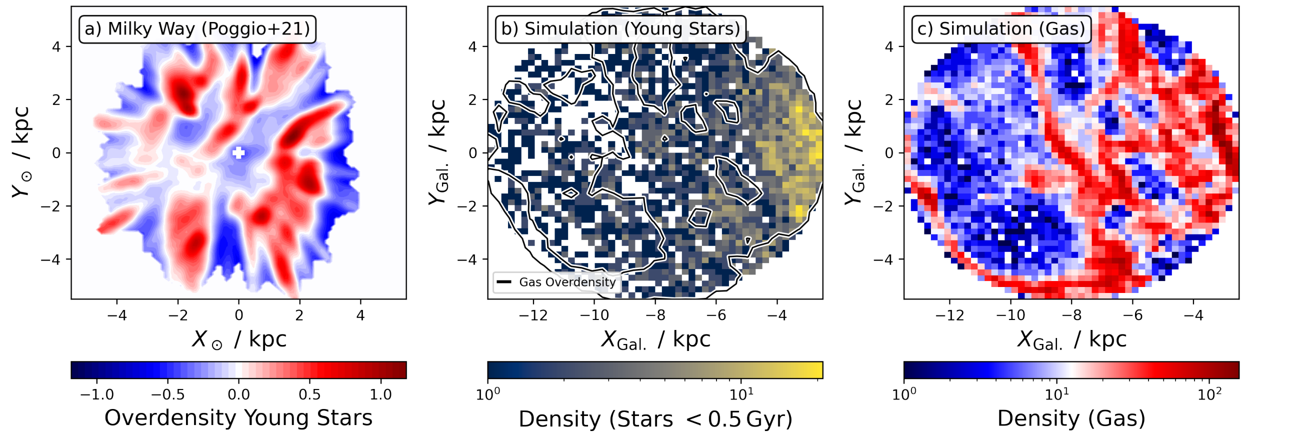

Figure 12. Comparison of density distribution of young stars and gas in the Milky Way and the NIHAO Milky Way analogue simulation. Panel a) shows the measurements of the Solar vicinity within 5 kpc by Poggio et al. (2021). Panels b) and c) show young stars and gas NIHAO, respectively, for a selected region similar to panel a). Black and white contour lines in panel b) trace overdensities in the gas distribution of panel c).

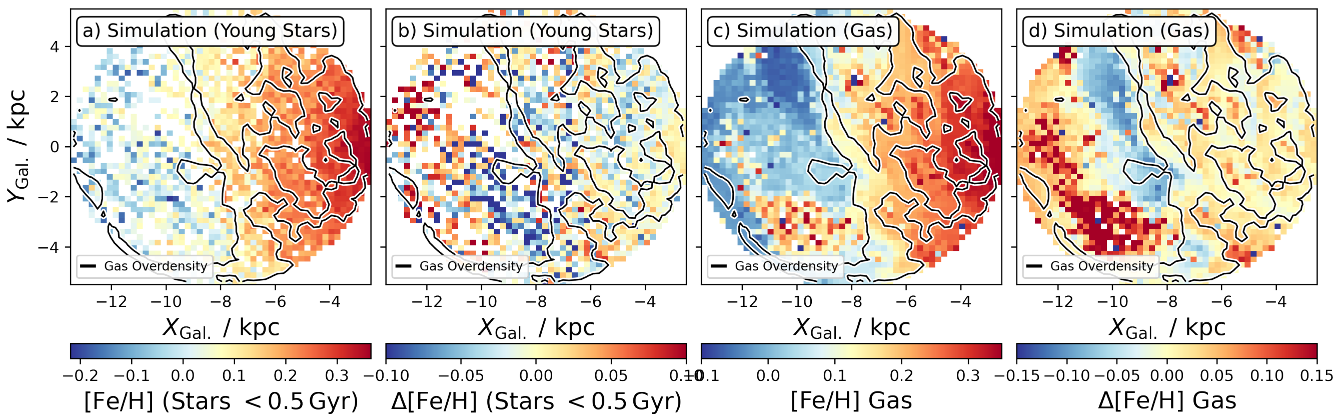

Figure 13. Comparison of density distribution of young stars and gas NIHAO Milky Way analogue simulation for the same regions as Figs. 12b and 12c. Panels a) and c) trace median gas and young star iron abundances, respectively. Panels b) and c) plot the residual [Fe/H] of gas and stars, respectively, when correcting with a radial metallicity gradient fit. Black and white contour lines in panel b) trace overdensities in the gas distribution of Fig. 12c).

the outer gas spiral (lower left of Fig. 13d) and −0.1 dex in [Fe/H] in front of the inner gas spiral (upper center of Fig. 13d) with a steep edge consistent with the gas spiral edge. We have identified the same patterns in both [Fe/H] and A(O) as both elements trace each other rather well in the simulation of young stars. Tentatively, we even see a slight enhancement of [Fe/H] at the trailing edge of the inner spiral arm (top of Fig. 13d). We convince ourselves of the step-like behaviour by selecting a small slit-like region of $\varphi_{\rm Gal.} \sim 0$ deg and $-2 < Y_{\rm Gal.}$ / kpc < -1 and tracing the gas metallicity and gas density as a function of radius in Fig. 14. We indeed find steps and confirm that they coincide with the location of significant gas overdensities. These step-patterns have also been found by Grand et al. (2015) in another simulation and observationally by Ho et al. (2017). In Fig. 14, we note an extended flat region just beyond $R_{\rm Gal.} > 10$ kpc, the best fitting $R_{\rm break}$ of an assumed piecewise linear fit.

Our analyses suggest that the correlation of void and overdensities with chemical enrichment of gas and young stars is more complicated and should better be followed up by tracing these structures over simulation look-back time in a dedicated follow-up analysis. This could also involve the tracing of star formation bursts and disk instabilities

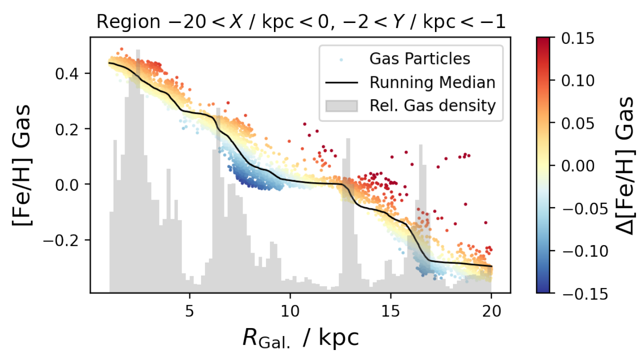

Figure 14. Radial gas metallicity gradient of a slit-like region ($-2 < Y_{\rm Gal.}$ / kpc < -1) from Fig. 13. The plot extends towards larger and smaller radii and shows the step-like distribution of individual gas particle metallicities colored by their deviation from a global fit. A running median along 1000 particles is shown as black line. The gray histogram indicates the gas density along the radius with prominent overdensities coinciding with step edges.

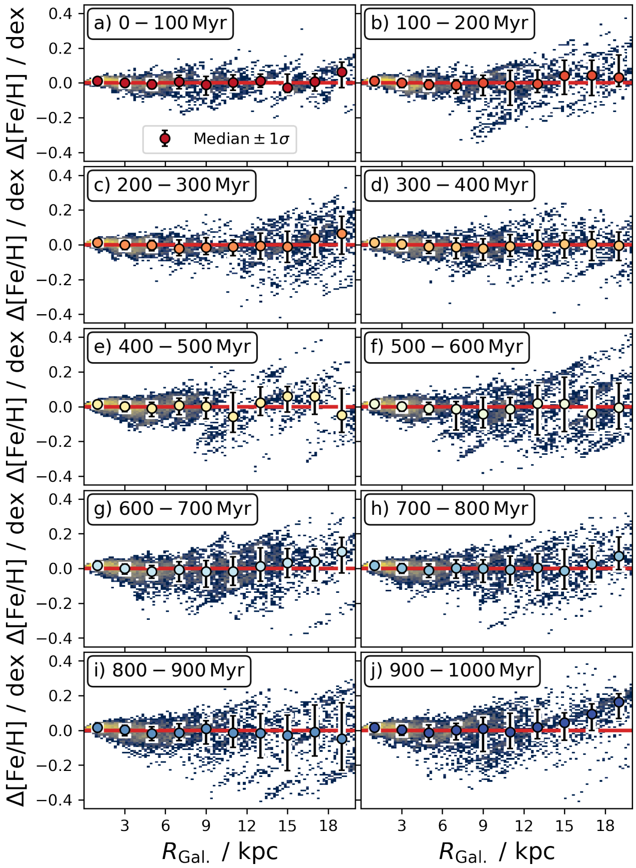

Figure 15. Stellar density distribution and spread of [Fe/H] across different galactocentric radii with respect to a global linear radial metallicity gradient across different age ranges. Panels a-j) show young stars and exhibit a rather similar trend, whereas the scatter increases significantly for stars above 0.5 Gyr in panels panels k) and l).

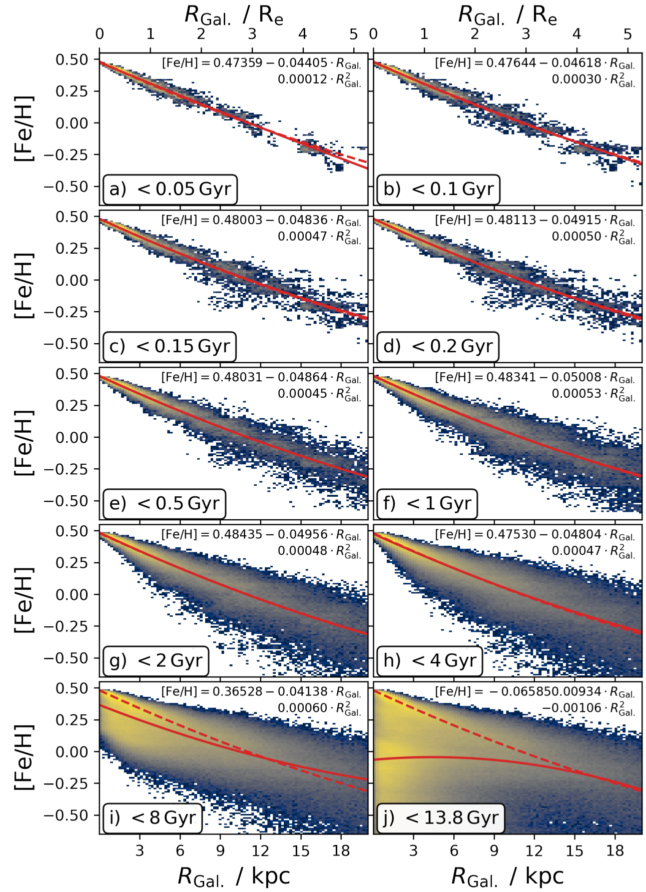

Figure 16. Radial metallicity gradients and quadratic fits for different maximum age ranges. The quadratic fit to stars below 0.5 Gyr as dashed red line for reference and the quadratic fit to each shown distribution is overlaid as solid red line with the functional form given as inset text.

(Sánchez et al. 2014; Sánchez-Blázquez et al. 2014; Ho et al. 2015) as well as tracing how much self-enrichment as well as mixing and dilution takes place around the gas spirals (Ho et al. 2017). Rather than going back in simulation time, the present simulation data of a single snapshot in time already allows us to look back in terms of stellar lifetime, as we discuss subsequently.

5.4 The impact of time and age: mixing and migration

Although we have chosen a rather small stellar age of 0.5 Gyrto trace the radial metallicity gradient without expected significant impact of radial mixing and migration, we are testing and discussing this particular choice in this section in two ways. Firstly, we test the deviation of the radial metallicity gradient from the same global shape as well as the abundance spread across a smaller age bins of 100 Myr between 0 – 1000 Myr in Fig. 15. Secondly, we trace the distribution of stellar metallicity across galactic radii for increasing age bins from 50 Myr up to the maximum stellar age of 13.8 Gyr in Fig. 16.

Our first test in in Fig. 15 shows that the deviation from a global trend does remain similar in functional form. We find that the spread of iron abundance does indeed scatter significantly, but the distributions stay within the same overall shape across the ten age bins. We note though, that the smallest age bin of 0 – 100 Myr shows the least abundance scatter.

This is consistent with the picture from our second test of increasing age ranges in Fig. 16. Here we find the first significant deviation from a tighter and already slightly quadratic relation for an age of 100 – 150 Myr in Fig. 16c - our previously identified Group 3. As expected from previous simulations and observations, we see an increase of the scatter as we include more and more older stars. We note a still similar albeit more scattered shape for stars below 4 Gyr in Fig. 16h, before we start to see a more metal-poor population of stars in the inner galaxy appear between 4 – 8 Gyr in Fig. 16i. These also start to significantly influence the quadratic fit to the radial metallicity distribution that show as red line in comparison to our reference fit shown red dashed line. The significant amount of metal-poor stars in the inner galaxy then completely tilts the distribution when also including stars between 8 – 13.8 Gyr in Fig. 16j.

While we cannot exclude radial migration playing a role for change of radius for the youngest stars of the simulation, since Frankel et al. (2018) predicted significant shifts even for ages below 0.5 Gyr (see their Fig. 10), the larger scatter for older stars certainly suggesting a larger (re-)distribution of stars along the radial axis, as found in previous simulations (Minchev & Famaey 2010; Grand et al. 2015).

5.5 Implications for Milky Way studies

Our analysis of the radial metallicity gradient in a simulated NIHAO-UHD galaxy offers several insights that are directly applicable to understanding the Milky Way's gradient.

First, the nature of the gradient - whether it is linear or better described by more complex functional forms - remains a critical question. Previous studies, such as those by Lépine et al. (2011) and Donor et al. (2020), have suggested the potential for a break radius, possibly at the corotation radius or further out (Scarano & Lépine 2013), which could indicate two distinct linear regimes. In our analysis, we find evidence that the gradient at least not purely linear, but could also be smoothly flattening. Applying a smooth quadratic function on observational data (Yong et al. 2012; Andrievsky et al. 2004; Genovali et al. 2014), might provide a better or at least consistent fit for the Milky Way data without the need for a break radius. However, even this may not fully capture the nuances observed in our simulations. Chemical evolution models propose that a more sophisticated behaviour (e.g. Chiappini et al. 2001; Kubryk et al. 2015), reflecting varying influences of galactic processes at different radii. Understanding this structure in the simulated galaxy provides a framework for interpreting similar complexities in the Milky Way.

Given these complexities, it is also essential to consider how local sampling biases might affect our understanding of the Milky Way's metallicity gradient. For instance, incomplete samples that omit low [Fe/H] clusters or stars could skew gradient estimates, as suggested by our comparisons in Figures 9a and 9b. Our results indicate that young cluster with lower (or higher) [Fe/H] than expected at a given radius could indicate the previous presence of a spiral arm (see our identified Groups in Figs. 7 and 8). Furthermore we caution that localised effects - both intrinsic and in terms of selection function - could also mimic non-linear shapes and more spatial coverage is needed in the Milky Way. Our results also indicate that older clusters, which have been found more frequently at larger distances than young cluster - are likely influenced by radial migration - and thus complicate the interpretation of these radial metallicity gradients (Magrini et al. 2009; Lépine et al. 2011).

Cosmological zoom-in simulations like NIHAO-UHD are approaching the resolution needed to examine regions analogous to the solar vicinity, though the star particle numbers and mass resolution remain a limiting factor. Nonetheless, we observe distinct patterns in the distribution of young stars and gas, including lower [Fe/H] in the leading edges of gas overdensities and higher [Fe/H] in the trailing edges, consistent with findings by Grand et al. (2016), Ho et al. (2017), and Kreckel et al. (2019). These trends suggest that local metallicity variations, driven by gas dynamics, may also play a significant role in shaping the observed gradients in the Milky Way.

Additionally, our study hints at the potential for more nuanced variations in [Fe/H] across different regions of the galaxy. In particular, the gas shows a step-like behavior of [Fe/H] changes around the edges of gas overdensities (Fig. 14), with significant deviations from the global gradient in specific regions. We have also found larger stellar void around $-12 < R_{\mathrm{Gal}} < -10$, kpc. Although further investigation is needed, these findings could have important implications for understanding localized star formation events and their impact on the overall metallicity distribution in the Milky Way (Sánchez et al. 2014; Sánchez-Blázquez et al. 2014; Ho et al. 2015). It will certainly be exciting to see how much more insights (Poggio et al. 2021; Hackshaw et al. 2024) we will get from the more extended data of future data releases of the *Gaia* and spectroscopic survey.

Finally, while we cannot directly link spiral arms to bar resonances or bar-driven mixing, because of a negligible bar strength in this galaxy[3] (but see Minchev & Famaey 2010; Di Matteo et al. 2013), the influence of a galactic bar on the spiral arms and, by extension, on the radial metallicity gradient, remains a possibility. Disk instabilities and warps might further complicate the interpretation of these gradients and progress will likely rely on the detailed disentangling of these effects from both cosmological as well as idealised simulations (Minchev et al. 2013; Grand et al. 2015, 2016; Bland-Hawthorn et al. 2024; Tepper-Garcia et al. 2024).

5.6 Implications for extragalactic studies

The insights gained from our analysis of the radial metallicity gradient in a simulated NIHAO-UHD galaxy extend beyond the Milky Way, offering valuable implications for the study of extragalactic systems.

One key observation is that deviations from a purely linear metallicity gradients, as seen in our Milky Way analogue, are common in other galaxies as well. When fitting a piecewise linear fit to our data, we found a break radius at $R_{\mathrm{Gal.}} = 10.0 \pm 0.5\,kpc$. Converted to effective radii $\mathrm{R_e}$ or radii $\mathrm{R_{25}}$ covering the 25 mag arcsec^{-2} isophote[4], this corresponds to $R_{\mathrm{break}} \sim 2.5\,\mathrm{R_e} \equiv 0.7\,\mathrm{R_{25}}$ for our simulation. This would be consistent with the observational results by Sánchez et al. (2014) who found that breaks in metallicity gradients are common in both spiral and barred galaxies, with flattening of the abundance being evident beyond $\sim 2\,\mathrm{R_e}$ (compare also to Belfiore et al. 2017). Similar to our suggestion for Milky Way studies, we suggest to also test a smooth function, such as a quadratic one, on extragalactic observational data (e.g. Chen et al. 2023; Bresolin et al. 2012) to test the preference of a distinct break radius.

Although the focus of this research lies on the observable region of the Milky Way ($R_{\mathrm{Gal.}} < 20\,\mathrm{kpc}$) and most other galaxies ($R_{\mathrm{Gal.}} < 2.5\,\mathrm{R_e}$), the finding of significant gradient changes in the outskirts of galaxies by Garcia et al. (2023), suggests to also test this region of our Milky Way analogue. Garcia et al. (2023, see their Fig. 4) found a metallicity floor in IllustrisTNG galaxies and when using their sample to identify a metallicity floor radius for a Milky Way mass galaxy with $\log(M_\star/\mathrm{M_\odot} = 10.7$ (Bland-Hawthorn & Gerhard 2016) at redshift $z \sim 0$, we would expect to find it around $25 - 30\,\mathrm{kpc}$. We therefore extend the analysed radius to $R_{\mathrm{Gal.}} \leq 100\,\mathrm{kpc}$ and indeed find a similar abundance floor of $\mathrm{[Fe/H]} \geq -0.64$ for young stars and $\mathrm{A(O)} \geq 8.12$ for the majority of gas (see Fig. 17 at a similar radius[5]. These lowest abundances remind us of two observational results. Firstly, the iron abundance floor is consistent with the lower end of the Milky Way thin - and coincidentally outer - disk of $\mathrm{[Fe/H]} \sim -0.7$ (Bensby et al. 2014; Buder et al. 2019). Secondly this oxygen abundance floor is consistent with the results by Grasha et al. (2022) from TYPHOON galaxy observations. Grasha et al. (2022) suggested this could be caused by changes in the ratio of supernovae II and AGB reflected by a changing ratio of nitrogen to oxygen abundance N/O which also flattens towards a lower plateau below metallicities of $A(O) \sim 8.0$ (Nicholls et al. 2017). While we cannot follow this observation up with the present simulation, a similar simulation used by Buder et al. (2024) has actually traced the relative contribution

[3] The second Fourier component of the density distribution has an amplitude of only 0.02.

[4] We follow Williams et al. (2009); Chen et al. (2023) and assume $\mathrm{R_{25}} = 3.6\,\mathrm{R_e}$.

[5] We append the a plot of the spatial distribution in Fig. B1 and note the galaxy without gas at a sufficiently large distance of 92 kpc, that is, $(Y, Y, Z) = (-50, -75, 20)$ kpc.

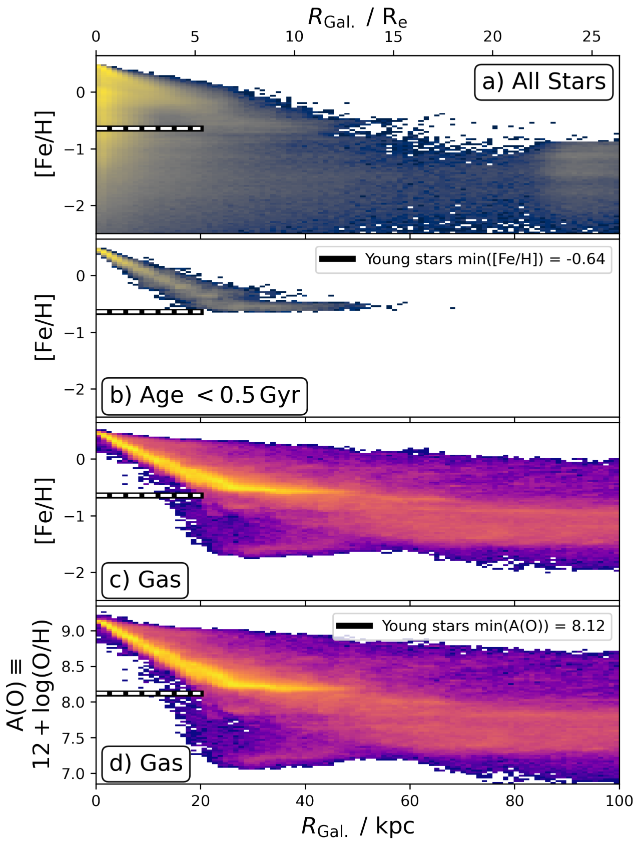

Figure 17. Radial metallicity functions for all stars (panel a), young stars (panel b), and gas (panels c and d for iron and oxygen as metallicity tracers) out to $R_{\mathrm{Gal.}} \leq 100$ kpc. Panels b and c are comparable to Figs. 2a and 10a for a smaller radial coverage.

of both supernovae II and AGB and should be used to test this hypothesis.

We note though, that the implemented chemical evolution of the NIHAO-UHD simulations are limited to the current incomplete knowledge of evolutionary pathways and yields (Buck et al. 2021) in addition to known shortcomings of the limited resolution and imperfect physics of cosmological zoom-in simulations (Buck 2020). Both could contribute to the identified differences in absolute and relative abundances across different scales - including a different scatter of abundances for example of the gas phase metallicity between our NIHAO-UHD of up to 0.1 dex and the low scatter of 0.03 – 0.05 dex (and even lower on local scales) found by PHANGS-MUSE face-on observations (Kreckel et al. 2020). Extending our analysis to other NIHAO simulations and further improving the resolution and physics of the simulations will be key in uniting the observational and theoretical insights into galactic chemical evolution on small and large scales.

Similar to more resolved and higher quality observations in the Milky Way, we also expect more, better, and diverse face-on and edge-on observations and analyses across a range of wavelengths by the PHANGS and GECKOS teams (Kreckel et al. 2019, 2020; van de Sande et al. 2023) as well as the SDSS-V and MAGPI collaborations (Kollmeier et al. 2017; Foster et al. 2021; Mun et al. 2024; Chen et al. 2024), among many other ongoing efforts.

6 CONCLUSIONS

6.1 Main Take-Away

- We have analysed the radial metallicity distribution of young stars and gas in the inner 20 kpcof a NIHAO-UHD Milky Way analogue (Fig. 1), finding a predominantly linear decrease (Fig. 2).
- Looking into the shape in more detail, we find that a piecewise linear and quadratic functions both perform better than a linear fit to the radial metallicity relation. However, we see no significant preference between piecewise and quadratic functions based on our assessments (Fig. 3). While the specific slopes differ when fitting all points or binned data, they agree within the still rather small fitting uncertainties.
- We find that a piecewise linear function can well mimic a quadratic function across the scales used in Milky Way and extragalactic studies. Local deviations become traceable below are spatial resolution of $\Delta R_{\mathrm{Gal.}} \leq 2$ kpc (Fig. 4).
- We see no strong correlations of deviations in the vertical direction across the whole simulation (Fig. 5). Such correlations could, however, be blurred by azimuthal effects, like the galactic warp, which needs to be disentangled in the azimuthal dimension.
- We find various deviations from the global trend in azimuthal direction, including gaps as well as isolated streaks of stars with similar [Fe/H] across $\Delta R_{\mathrm{Gal.}} = 2-6$ kpc (Fig. 6). These can introduce local over- and under-enhancement of up to ±0.2 dex in [Fe/H] at a given radius.
- We find significant scatter across the radial metallicity distribution caused by streaks of stars born with similar [Fe/H] at similar times and similar but slightly extended regions of the galaxy (Figs. 7 and 8).
- Our results imply the need for a more careful consideration of local instrinsic and selection effects on radial metallicity gradient and scatter studies in the Milky Way (Fig. 9).
- We perform a preliminary comparison of observed and simulated young stars as well as simulated gas distribution and chemistry (Figs. 11 and 12), finding significant step-like changes in the gas chemistry at the leading and trailing edges of gas spirals, with lower and higher enhancement respectively (Figs. 13 and 14).
- We have further identified that the abundance scatter, which increases towards larger radii, is as large as 0.1 dex and already present at youngest ages of 100 Myr (Fig. 15). While not the focus of our analysis, we have also confirmed that the scatter significantly increases towards larger ages (Fig. 16).
- We have discussed the implications of our findings for studies of the Milky Way (Section 5.5) as well as external galaxies (Section. 5.6). Here, we firstly suggest to explore the spread of abundances across different radii in more detail. Secondly, we suggest to approach the fitting of gradients in external galaxies in a more agnostic to the shape. This will be particularly interesting when we can observe the outermost regions of galaxies, where simulations predict an abundance floor (Fig. 17).

6.2 Future Research

- Trace spatial and chemical coherence of over- and underdensities over times. Do this both across a range of stellar ages at redshift zero, but also when looking back at higher redshifts.
- higher mass resolution would help to overcome small sample sizes for comparison with Milky Way.
- We assumed that the modelled chemistry is fully accurate. While previous works are showing that relative trends for several elements

agree, we are still missing some of the details on the origin of elements, such as a complete picture of the synthesis sites, environments, and yields for elements. detailed physics?

- our study is making deductions based on a simulated Milky Way analogue, but the reality in both the actual Milky Way and other Milky Way analogues with slightly different nuances like merger history as well as bar and spiral arm strengths might lead to a different slightly or vastly radial metallicity relation.
- Potential Break radius around $R_\mathrm{Gal.} \sim 10\,\mathrm{kpc} \sim 2.5\,\mathrm{R_e}$ is still enigmatic. More studies needed to establish a link to a physical mechanism.
- It has to be seen what functional shape this radial metallicity relation is actually having, but our results are certainly encouraging to not only apply piecewise linear fits to galactic and extragalactic radial metallicity measurements.

ACKNOWLEDGEMENTS

We acknowledge the traditional owners of the land on which the ANU stands, the Ngunnawal and Ngambri people. We pay our respects to elders past, and present and are proud to continue their tradition of surveying the night sky and its mysteries to better understand our Universe.

This work was supported by the Australian Research Council Centre of Excellence for All Sky Astrophysics in 3 Dimensions (ASTRO 3D), through project number CE170100013. SB and KG acknowledge support from the Australian Research Council under grant numbers DE240100150 and DE220100766, respectively. TB acknowledges funding from the Carl Zeiss Stiftung and support from the European Research Council under ERC-CoG grant CRAGSMAN-646955. We gratefully acknowledge the Gauss Centre for Supercomputing e.V. (`www.gauss-centre.eu`) for funding this project by providing computing time on the GCS Supercomputer SuperMUC at Leibniz Supercomputing Centre (`www.lrz.de`). Simulations were partially computed with High Performance Computing resources at New York University, Abu Dhabi.

SOFTWARE

The research for this publication was coded in PYTHON (version 3.7.4) and included its packages ASTROPY (v. 3.2.2; Astropy Collaboration et al. 2013, 2018), IPYTHON (v. 7.8.0; Pérez & Granger 2007), MATPLOTLIB (v. 3.1.3; Hunter 2007), NUMPY (v. 1.17.2; Walt et al. 2011), PYNBODY (v. 1.1.0; Pontzen et al. 2013), SCIPY (v. 1.3.1; Virtanen et al. 2020), SKLEARN (v. 1.5.1 Pedregosa et al. 2011) STATSMODELS (v. 0.14.2 Perktold et al. 2024) We further made use of TOPCAT (version 4.7; Taylor 2005);

DATA AVAILABILITY

All code and data to reproduce the analysis and figures can be publically accessed via `https://github.com/svenbuder/nihao_radial_metallicity_gradients`.

The repository also includes the chemical and kinematic data of the simulated Milky Way analogue `g8.26e11` for last snapshot of the simulation for the observable footprint that were used for this study as well as the cleaned catalogue of GALAH DR3. All GALAH DR3 data is also published by Buder et al. (2021) and can be accessed publicly via `https://docs.datacentral.org.au/galah/dr3/overview/`. The full simulation data of `g8.26e11` can be obtained upon reasonable request from the authors. Currently the only limitation in making all data public is limited cloud space to host the data. We encourage interested readers to get in contact with the authors for full data access. Redshift zero snapshots from the original NIHAO-UHD simulations can be found here: `https://tobias-buck.de/#sim_data`.

If you are using either of these data to follow up on this research, remember to give appropriate credit to the researchers who created and curated either data set, that is, at least to Buder et al. (2021, 2022) and Buck et al. (2020, 2021).

REFERENCES

Agertz O., et al., 2021, MNRAS, 503, 5826
Allende Prieto C., Beers T. C., Wilhelm R., Newberg H. J., Rockosi C. M., Yanny B., Lee Y. S., 2006, ApJ, 636, 804
Anders F., et al., 2014, A&A, 564, A115
Anders F., et al., 2017, A&A, 600, A70
Andrievsky S. M., et al., 2002a, A&A, 381, 32
Andrievsky S. M., Bersier D., Kovtyukh V. V., Luck R. E., Maciel W. J., Lépine J. R. D., Beletsky Y. V., 2002b, A&A, 384, 140
Andrievsky S. M., Luck R. E., Martin P., Lépine J. R. D., 2004, A&A, 413, 159
Astropy Collaboration et al., 2013, A&A, 558, A33
Astropy Collaboration et al., 2018, AJ, 156, 123
Belfiore F., et al., 2016, MNRAS, 461, 3111
Belfiore F., et al., 2017, MNRAS, 469, 151
Bellardini M. A., Wetzel A., Loebman S. R., Faucher-Giguère C.-A., Ma X., Feldmann R., 2021, MNRAS, 505, 4586
Bellardini M. A., Wetzel A., Loebman S. R., Bailin J., 2022, MNRAS, 514, 4270
Bensby T., Feltzing S., Oey M. S., 2014, A&A, 562, A71
Bergemann M., et al., 2014, A&A, 565, A89
Binney J., Tremaine S., 2008, Galactic Dynamics: Second Edition. Princeton University Press
Bird J. C., Kazantzidis S., Weinberg D. H., Guedes J., Callegari S., Mayer L., Madau P., 2013, ApJ, 773, 43
Bland-Hawthorn J., Gerhard O., 2016, ARA&A, 54, 529
Bland-Hawthorn J., Tepper-Garcia T., Agertz O., Federrath C., 2024, ApJ, 968, 86
Boeche C., et al., 2013, A&A, 559, A59
Bresolin F., Kennicutt R. C., Ryan-Weber E., 2012, ApJ, 750, 122
Buck T., 2020, MNRAS, 491, 5435
Buck T., Macciò A. V., Dutton A. A., Obreja A., Frings J., 2019, MNRAS, 483, 1314
Buck T., Obreja A., Macciò A. V., Minchev I., Dutton A. A., Ostriker J. P., 2020, MNRAS, 491, 3461
Buck T., Rybizki J., Buder S., Obreja A., Macciò A. V., Pfrommer C., Steinmetz M., Ness M., 2021, MNRAS, 508, 3365
Buck T., Obreja A., Ratcliffe B., Lu Y., Minchev I., Macciò A. V., 2023, MNRAS, 523, 1565
Buder S., et al., 2019, A&A, 624, A19
Buder S., et al., 2021, MNRAS, 506, 150
Buder S., et al., 2022, MNRAS, 510, 2407
Buder S., Mijnarends L., Buck T., 2024, MNRAS, 532, 1010
Cantat-Gaudin T., Anders F., 2020, A&A, 633, A99
Casamiquela L., et al., 2019, MNRAS, 490, 1821
Chabrier G., 2003, PASP, 115, 763
Chen Q.-H., Grasha K., Battisti A. J., Kewley L. J., Madore B. F., Seibert M., Rich J. A., Beaton R. L., 2023, MNRAS, 519, 4801
Chen Q.-H., et al., 2024, MNRAS, 527, 2991
Chiappini C., 2002, Ap&SS, 281, 253
Chiappini C., Matteucci F., Gratton R., 1997, ApJ, 477, 765
Chiappini C., Matteucci F., Romano D., 2001, ApJ, 554, 1044
Chieffi A., Limongi M., 2004, ApJ, 608, 405
Chiosi C., 1980, A&A, 83, 206

Cunha K., et al., 2016, Astronomische Nachrichten, 337, 922
Di Matteo P., Haywood M., Combes F., Semelin B., Snaith O. N., 2013, A&A, 553, A102
Donor J., et al., 2020, AJ, 159, 199
Foster C., et al., 2021, Publ. Astron. Soc. Australia, 38, e031
Frankel N., Rix H.-W., Ting Y.-S., Ness M., Hogg D. W., 2018, ApJ, 865, 96
Frankel N., Sanders J., Ting Y.-S., Rix H.-W., 2020, arXiv e-prints, p. arXiv:2002.04622
Gaia Collaboration et al., 2016, A&A, 595, A1
Garcia A. M., et al., 2023, MNRAS, 519, 4716
Genovali K., et al., 2014, A&A, 566, A37
Graf R. L., Wetzel A., Bellardini M. A., Bailin J., 2024, arXiv e-prints, p. arXiv:2402.15614
Grand R. J. J., Kawata D., Cropper M., 2015, MNRAS, 447, 4018
Grand R. J. J., et al., 2016, MNRAS, 460, L94
Grasha K., et al., 2022, ApJ, 929, 118
Hackshaw Z., Hawkins K., Filion C., Horta D., Laporte C. F. P., Carr C., Price-Whelan A. M., 2024, arXiv e-prints, p. arXiv:2405.18120
Hayden M. R., et al., 2014, AJ, 147, 116
Hayden M. R., et al., 2015, ApJ, 808, 132
Hemler Z. S., et al., 2021, MNRAS, 506, 3024
Ho I. T., Kudritzki R.-P., Kewley L. J., Zahid H. J., Dopita M. A., Bresolin F., Rupke D. S. N., 2015, MNRAS, 448, 2030
Ho I. T., et al., 2017, ApJ, 846, 39
Hogg D. W., Eilers A.-C., Rix H.-W., 2019, AJ, 158, 147
Hunter J. D., 2007, Comput Sci Eng, 9, 90
Imig J., et al., 2023, ApJ, 954, 124
Janes K. A., 1979, ApJS, 39, 135
Karakas A. I., Lugaro M., 2016, ApJ, 825, 26
Katz D., Soubiran C., Cayrel R., Barbuy B., Friel E., Bienaymé O., Perrin M. N., 2011, A&A, 525, A90
Kauffmann G., 1996, MNRAS, 281, 475
Khoperskov S., Sivkova E., Saburova A., Vasiliev E., Shustov B., Minchev I., Walcher C. J., 2023, A&A, 671, A56
Knollmann S. R., Knebe A., 2009, ApJS, 182, 608
Kollmeier J. A., et al., 2017, arXiv e-prints, p. arXiv:1711.03234
Kreckel K., et al., 2019, ApJ, 887, 80
Kreckel K., et al., 2020, MNRAS, 499, 193
Kubryk M., Prantzos N., Athanassoula E., 2015, A&A, 580, A126
Lacey C. G., Fall S. M., 1985, ApJ, 290, 154
Larson R. B., 1976, MNRAS, 176, 31
Lemasle B., François P., Bono G., Mottini M., Primas F., Romaniello M., 2007, A&A, 467, 283
Lemasle B., François P., Piersimoni A., Pedicelli S., Bono G., Laney C. D., Primas F., Romaniello M., 2008, A&A, 490, 613
Lemasle B., et al., 2013, A&A, 558, A31
Lemasle B., et al., 2022, A&A, 668, A40
Lépine J. R. D., et al., 2011, MNRAS, 417, 698
Lilly S. J., Carollo C. M., Pipino A., Renzini A., Peng Y., 2013, ApJ, 772, 119
Lu Y., Buck T., Minchev I., Ness M. K., 2022, MNRAS, 515, L34
Ma X., Hopkins P. F., Feldmann R., Torrey P., Faucher-Giguère C.-A., Kereš D., 2017a, MNRAS, 466, 4780
Ma X., Hopkins P. F., Wetzel A. R., Kirby E. N., Anglés-Alcázar D., Faucher-Giguère C.-A., Kereš D., Quataert E., 2017b, MNRAS, 467, 2430
Magrini L., Sestito P., Randich S., Galli D., 2009, A&A, 494, 95
Magrini L., et al., 2017, A&A, 603, A2
Matteucci F., ed. 2001, The chemical evolution of the Galaxy Astrophysics and Space Science Library Vol. 253, doi:10.1007/978-94-010-0967-6.
Metha B., Trenti M., Chu T., 2021, MNRAS, 508, 489
Minchev I., Famaey B., 2010, ApJ, 722, 112
Minchev I., Chiappini C., Martig M., 2013, A&A, 558, A9
Minchev I., Chiappini C., Martig M., 2014, A&A, 572, A92
Minchev I., et al., 2018, MNRAS, 481, 1645
Moran S. M., et al., 2012, ApJ, 745, 66
Mun M., et al., 2024, MNRAS, 530, 5072
Myers N., et al., 2022, AJ, 164, 85
Nicholls D. C., Sutherland R. S., Dopita M. A., Kewley L. J., Groves B. A., 2017, MNRAS, 466, 4403
Obreja A., Buck T., Macciò A. V., 2022, A&A, 657, A15
Pedregosa F., et al., 2011, J Mach Learn Res, 12, 2825
Pérez F., Granger B. E., 2007, Comput Sci Eng, 9, 21
Perktold J., et al., 2024, statsmodels/statsmodels: Release 0.14.2, doi:10.5281/zenodo.593847
Pilkington K., et al., 2012, A&A, 540, A56
Pilyugin L. S., 2003, A&A, 397, 109
Pilyugin L. S., Tautvaišienė G., 2024, A&A, 682, A41
Pilyugin L. S., Grebel E. K., Zinchenko I. A., Nefedyev Y. A., Vílchez J. M., 2017, A&A, 608, A127
Planck Collaboration et al., 2014, A&A, 571, A16
Poggio E., et al., 2018, MNRAS, 481, L21
Poggio E., et al., 2021, A&A, 651, A104
Poggio E., et al., 2022, A&A, 666, L4
Pontzen A., Roškar R., Stinson G. S., Woods R., 2013, pynbody: Astrophysics Simulation Analysis for Python, Astrophysics Source Code Library, record ascl:1305.002
Quirk W. J., Tinsley B. M., 1973, ApJ, 179, 69
Ratcliffe B. L., Ness M. K., Buck T., Johnston K. V., Sen B., Beraldo e Silva L., Debattista V. P., 2022, ApJ, 924, 60
Ratcliffe B., et al., 2023, MNRAS, 525, 2208
Rolleston W. R. J., Smartt S. J., Dufton P. L., Ryans R. S. I., 2000, A&A, 363, 537
Rosales-Ortega F. F., Díaz A. I., Kennicutt R. C., Sánchez S. F., 2011, MNRAS, 415, 2439
Rybizki J., Just A., Rix H.-W., 2017, A&A, 605, A59
Sánchez-Blázquez P., et al., 2014, A&A, 570, A6
Sánchez-Menguiano L., et al., 2016, A&A, 587, A70
Sánchez S. F., et al., 2013, A&A, 554, A58
Sánchez S. F., et al., 2014, A&A, 563, A49
Scarano S., Lépine J. R. D., 2013, MNRAS, 428, 625
Schönrich R., Binney J., 2009, MNRAS, 396, 203
Searle L., 1971, ApJ, 168, 327
Seitenzahl I. R., et al., 2013, MNRAS, 429, 1156
Sharda P., Krumholz M. R., Wisnioski E., Forbes J. C., Federrath C., Acharyya A., 2021, MNRAS, 502, 5935
Shaver P. A., McGee R. X., Newton L. M., Danks A. C., Pottasch S. R., 1983, MNRAS, 204, 53
Spina L., et al., 2021, MNRAS, 503, 3279
Stanghellini L., Magrini L., Casasola V., 2015, ApJ, 812, 39
Stinson G., Seth A., Katz N., Wadsley J., Governato F., Quinn T., 2006, MNRAS, 373, 1074
Stinson G. S., Brook C., Macciò A. V., Wadsley J., Quinn T. R., Couchman H. M. P., 2013, MNRAS, 428, 129
Taylor M. B., 2005, ASPC, 347, 29
Tepper-Garcia T., Bland-Hawthorn J., Vasiliev E., Agertz O., Teyssier R., Federrath C., 2024, arXiv e-prints, p. arXiv:2406.00342
Tinsley B. M., 1980, Fundamentals Cosmic Phys., 5, 287
Tissera P. B., Rosas-Guevara Y., Bower R. G., Crain R. A., del P Lagos C., Schaller M., Schaye J., Theuns T., 2019, MNRAS, 482, 2208
Twarog B. A., 1980, ApJ, 242, 242
Twarog B. A., Ashman K. M., Anthony-Twarog B. J., 1997, AJ, 114, 2556
Vickers J. J., Shen J., Li Z.-Y., 2021, ApJ, 922, 189
Vilchez J. M., Esteban C., 1996, MNRAS, 280, 720
Virtanen P., et al., 2020, Nature Methods, 17, 261
Wadsley J. W., Keller B. W., Quinn T. R., 2017, MNRAS, 471, 2357
Walt S. v. d., Colbert S. C., Varoquaux G., 2011, Comput Sci Eng, 13, 22
Wang L., Dutton A. A., Stinson G. S., Macciò A. V., Penzo C., Kang X., Keller B. W., Wadsley J., 2015, MNRAS, 454, 83
Willett E., et al., 2023, MNRAS, 526, 2141
Williams M. J., Bureau M., Cappellari M., 2009, MNRAS, 400, 1665
Wyse R. F. G., Silk J., 1989, ApJ, 339, 700
Yong D., Carney B. W., Friel E. D., 2012, AJ, 144, 95
Zari E., Hashemi H., Brown A. G. A., Jardine K., de Zeeuw P. T., 2018, A&A, 620, A172

Zari E., Rix H. W., Frankel N., Xiang M., Poggio E., Drimmel R., Tkachenko A., 2021, A&A, 650, A112
Zaritsky D., Kennicutt Robert C. J., Huchra J. P., 1994, ApJ, 420, 87
van de Sande J., Fraser-McKelvie A., Fisher D. B., Martig M., Hayden M. R., the GECKOS Survey collaboration 2023, arXiv e-prints, p. arXiv:2306.00059

Table A1. Global linear gradient fit results with different methods. LinearRegression is part of the sklearn package.

Method	Intercept ($a_0 \pm \sigma_{a_0}$)	Slope ($a_1 \pm \sigma_{a_1}$)
statsmodels.api.ODR	0.46266 ± 0.00039	-0.04109 ± 0.00005
scipy.odr	0.46268 ± 0.00039	-0.04109 ± 0.00005
np.polyfit	0.46266 ± 0.00039	-0.04109 ± 0.00005
LinearRegression	0.46268 ± 0.00016	-0.04108 ± 0.00006
scipy.curve_fit	0.46266 ± 0.00039	-0.04109 ± 0.00005

APPENDIX A: TESTING DIFFERENT FITTING ROUTINES

Table A1

APPENDIX B: INTERESTING BUT NOT MAIN FOCUS OF THIS PAPER

Fig. B1 for an extended $R_\mathrm{Gal.} \leq 100\,\mathrm{kpc}$ and $|z_\mathrm{Gal.}| \leq 50\,\mathrm{kpc}$.

Figs. B2 and B3

Fig. B4

APPENDIX C: SUPPLEMENTARY MATERIAL

Fig. C1: showing residuals, but not really adding much more than Fig. 6 already did. So take out completely or add as supplementary material?

This paper has been typeset from a TEX/LATEX file prepared by the author.

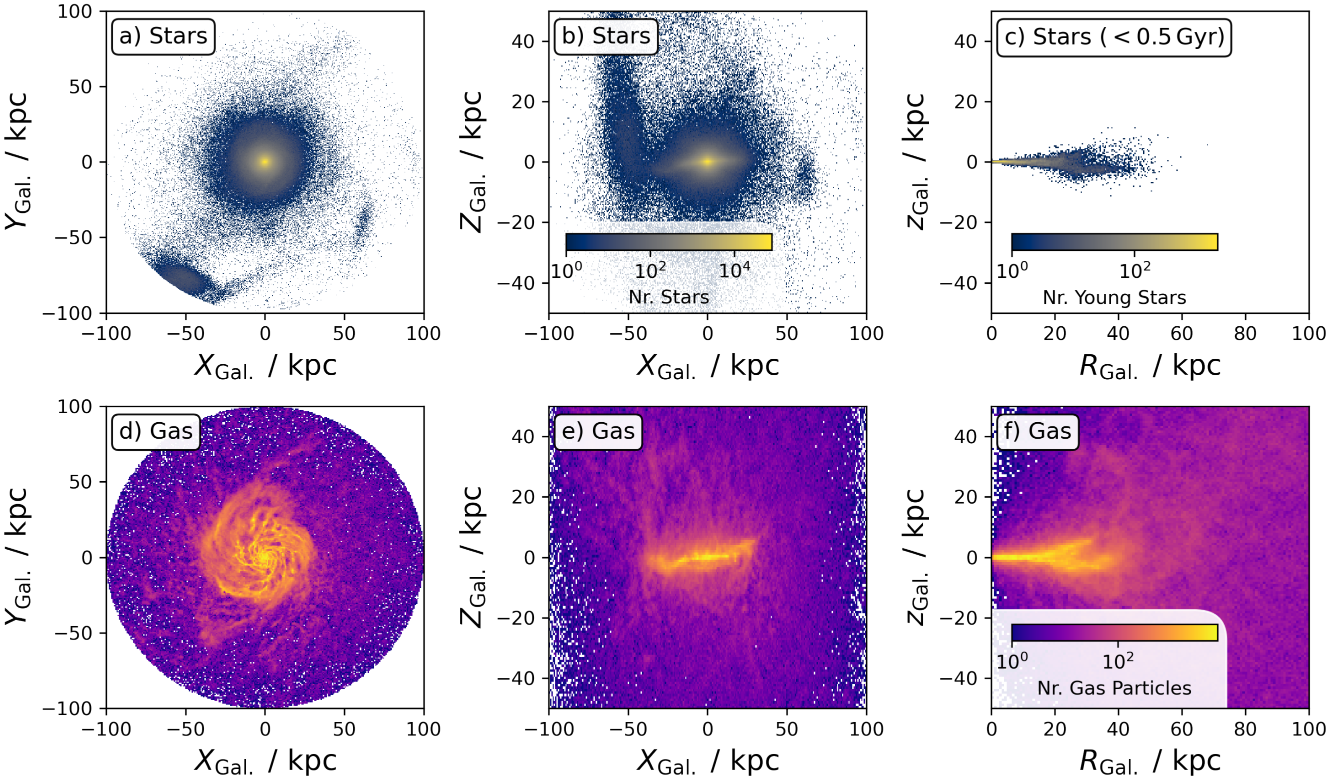

Figure B1. Same as Fig. 1, but for an extended $R_{\mathrm{Gal.}} \leq 100\,\mathrm{kpc}$ and $|z_{\mathrm{Gal.}}| \leq 50\,\mathrm{kpc}$.

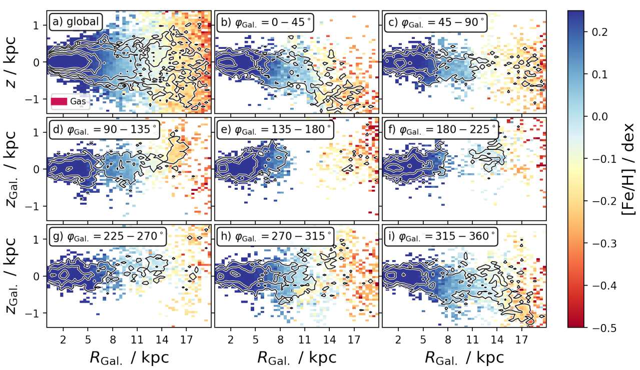

Figure B2. Tracing young stars' iron abundance [Fe/H] across galactocentric radii $R_{\mathrm{Gal.}}$ and height $z_{\mathrm{Gal.}}$ across the whole galaxy (panel a) and different azimuthal ranges/sectors (panels b-i).

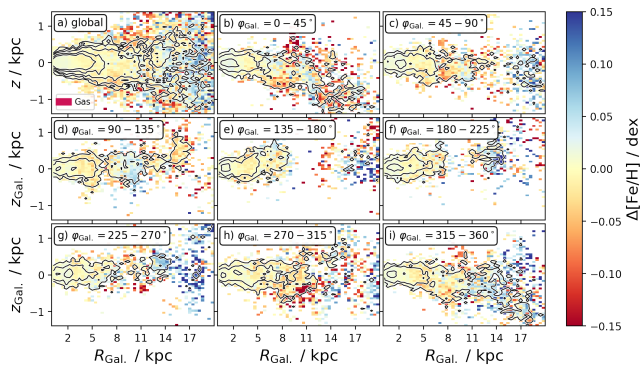

Figure B3. Tracing young stars' iron abundance [Fe/H] residuals (relative to global gradient) across galactocentric radii $R_{\mathrm{Gal.}}$ and height $z_{\mathrm{Gal.}}$ across the whole galaxy (panel a) and different azimuthal ranges/sectors (panels b-i).

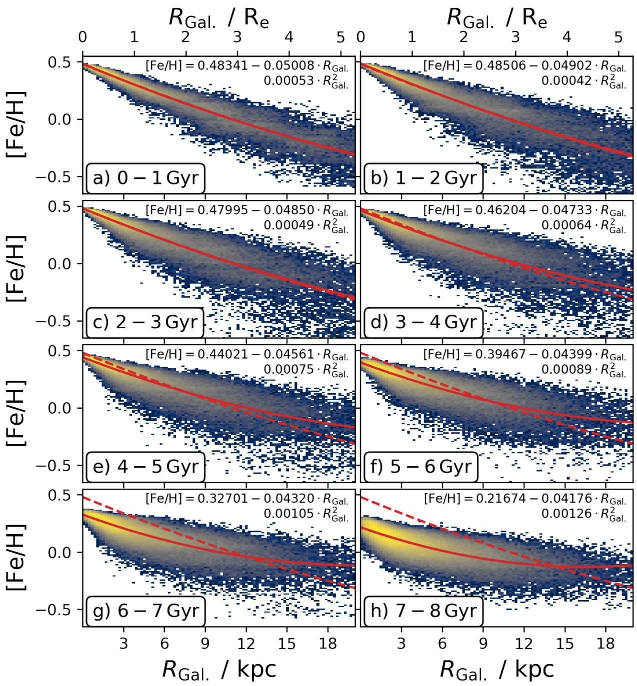

Figure B4. Radial metallicity gradients and quadratic fits for 1 Gyr age bins.

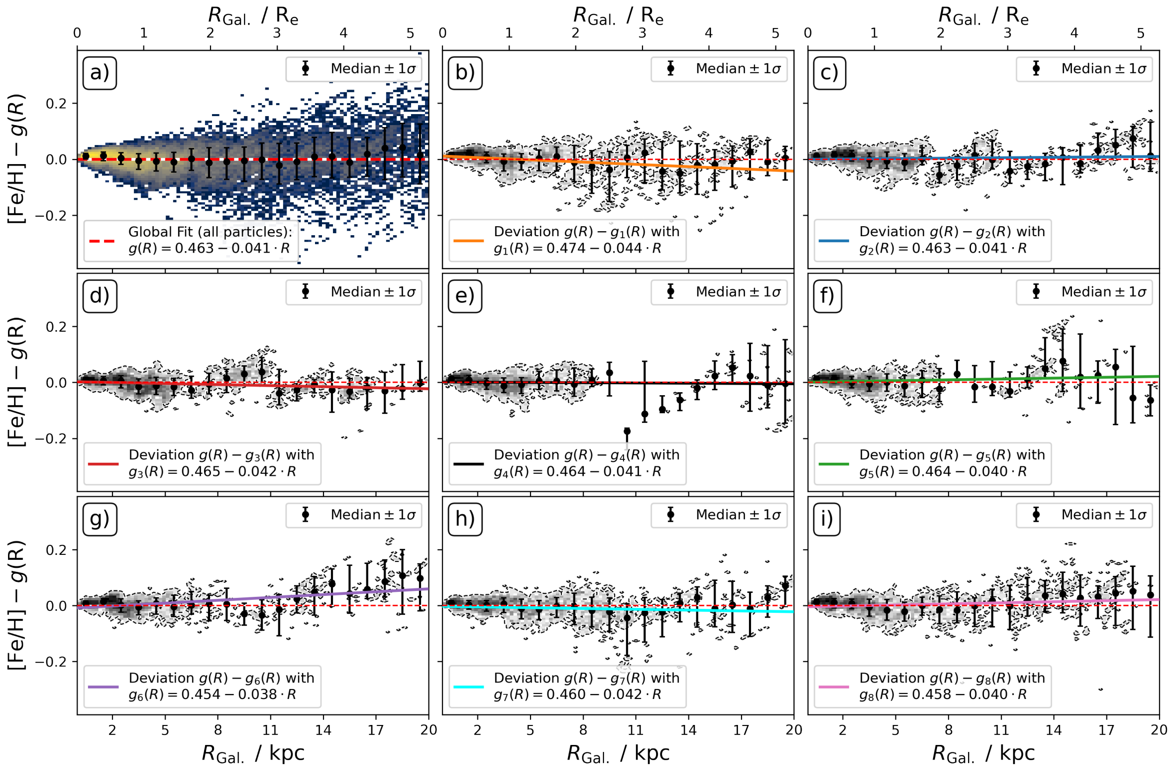

Figure C1. Stellar density variation of the radial metallicity gradient R − [Fe/H] across full stellar disk (panel a) and 8 different sectors (same panel order as for Fig. 6). Linear radial metallicity gradients have been fit globally (red dashed line) and for each sector with colors following the same color code as in Fig. 6.